

AN ALMA SURVEY OF SUB-MILLIMETRE GALAXIES IN THE EXTENDED CHANDRA DEEP FIELD SOUTH: A BLIND SEARCH FOR EMISSION LINES AT 145 GHZ



MINOR RESEARCH PROJECT IN ASTRONOMY

Presented by:

JORGE ANDRÉS VILLA VÉLEZ

To obtain the MSc. Astronomy degree

Advisor

Dr. Jacqueline A. Hodge

Second Reader

Dr. Paul van der Werf



Universiteit
Leiden
Sterrewacht Leiden

Universiteit Leiden - Sterrewacht Leiden
Faculteit Wiskunde en Natuurwetenschappen
2017

ABSTRACT

We present Atacama Large Millimeter/submillimeter Array (ALMA) band 4 (145 GHz) observations of 51 ALESS sources. A CO(4 → 3)-emission line for ALESS070.1 and ALESS122.1 at 138.88 ± 0.02 GHz and 152.44 ± 0.01 GHz was detected respectively. Our CO detections have a good signal-to-noise ratio reaching $\sim 6\sigma$ and $\sim 10\sigma$ for both sources. We measured the line luminosity through this transition and estimate the amount of molecular gas to be in terms of the CO-to-M_{H₂} conversion factor, $M_{H_2} = (11.74 \pm 4.76) 10^{10} M_\odot \alpha_{CO}$ and $M_{H_2} = (13.56 \pm 4.29) 10^{10} M_\odot \alpha_{CO}$ for each source. In the case of ALESS122.1 we found the CO luminosity ratio to be $r_{41} = 0.32 \pm 0.01$ after comparing our integrated luminosity for CO(4 → 3) to the CO(1 → 0) reported in literature. Our derived spectroscopic redshift of $z \sim 2.0252$ and the measured molecular mass for ALESS122.1 are consistent with previous observations. The redshift measured for ALESS070.1 corresponds to $z \sim 2.3197$ and represents a plausible solution to a discrepancy in previous measurements obtained from the optic spectroscopy. An estimation of the dynamical mass for both sources and implications of the CO-SLED for ALESS122.1 were also addressed.

Key words: *Submillimeter galaxies - (SMGs), ALESS-survey, CO line emission, Spectroscopic redshift, Molecular mass.*

*Wat mij betreft weet ik niets zeker,
maar naar de sterren kijken zet me aan het dromen.*

—Vincent Willem van Gogh
(1853 - 1890) Dutch Post-Impressionist painter.

ACKNOWLEDGMENTS

First and foremost I would like to thank my supervisor, Dr. Jacqueline Hodge who encouraged me to research in a completely different and beautiful branch of Astronomy as it is the Radio Astronomy. I am extremely grateful for all the new things she taught me in order to be a good researcher and to pave my way as a scientist.

To my parents, Jorge Mario Villa Marín and Gladys Vélez Muñoz who have trusted in me through this years, always supporting all my dreams and also now in this adventure. They have always been an important shoulder I can rely on to take every step forward on my way to be a good scientist. To all my family in Colombia and USA because this dream would have not been becoming real without their enormous help and trust in me.

Also, to Paula Andrea Ortíz Otálvaro who helped me to get rapidly involved in the Dutch life-style and feel Leiden as a second home since the first day. To my fellow master Colombian friends Juan Manuel Espejo Salcedo and Andrés Felipe Ramos Padilla for all those good times lived inside and outside the university. For all those enriching talks which shed light when problems seemed to have no solution. Someone, who motivated me to study and to look forward, Guadalupe Cañas Herrera, my little Spanish friend, thanks for all those good advises and funny times.

My dutch friends which helped me to feel this country as a second home, for all those good times and memories that will be forever in my mind (Michelle Willebrands, Esmee Stoop, Charlotte Brand, Lieke van Son, Marco Trueba van den Boom, Job van der Wardt, Dennis Vaendel, Lennart van Sluijs, Martijn Oei and Dirk van Dam). I would also like to dedicate this to my fellow international master friends who came here to make the same dream come true, Louis Martin, Michail Dagtzis and Pranav Kumar Mohanty. Last but not least, to Sofia Sarperi and Riccardo Mattia Baldo which I had the pleasure to meet during their Erasmus program in Leiden. To them, a big thank for all the good moments and conversations.

When I arrived to Leiden I thought it was going to be impossible to keep on doing the things I used to in Medellín. However I met a group of beautiful people who accepted me and shared all their empathy with me. To the Chileans Valeria Olivares, Pedro Salas, Pablo Castellanos, Heather Andrews, Javiera Paz, Sebastián Rumie and Nicolás Salinas. Also to my Mexican friend Santiago Torres, my Colombian friends Lina Bayona and Diana Aranzales who always took care of me. To one person who was always there to support and encourage me, my Portuguese friend Marta Figueiredo. To Dennis Hiltrop the kindest German I have ever met, with whom I had enriching talks.

Before coming to The Netherlands I was going through a bad time and now that I am here witnessing this dream coming true I really need to thank to my cousin Jaime Muñoz and his family because they took care of me in California in one of my darkest times, helping and cheering me up. They always encouraged me to continue straight on the science path, being humble and never backing off.

To all the people who directly or indirectly made this first step on my way to get a master in Astronomy possible, many many thanks and I will keep on fighting until the end on my way to keep on reaching my dreams.

CONTENT

1	THEORETICAL FRAMEWORK	1
1.1	Introduction	1
1.2	Submillimeter-Luminous Galaxies (SMGs)	1
1.3	SED	2
1.3.1	Continuum Emission From Dust	4
1.3.2	Line Emission	5
1.4	Molecule transitions	6
1.4.1	CO emission	6
1.4.2	HCN, [CI] and [CII] emission	9
1.5	ALESS Survey	10
2	OBSERVATIONAL DATA: FINAL SAMPLE	13
2.1	Introduction	13
2.2	Sample of Galaxies and calibration	13
2.3	Imaging	14
2.4	Final Sample	15
3	SPECTRAL LINE ANALYSIS	21
3.1	Introduction	21
3.2	Spectrum Extraction	21
3.3	Line Fitting	22
3.3.1	χ^2 difference and goodness of fit	24
3.3.2	Acceptance method and Fitting parameters	26
3.3.3	Spectroscopic redshift for ALESS070.1	29
3.4	Imaging: Continuum, line and IR counterpart	31
4	RESULTS AND DISCUSSION	35
4.1	Introduction	35
4.2	CO luminosity and molecular mass	35
4.3	SLED for ALESS122.1	37
4.4	Discussion	39
4.5	Future Work	40
5	SUMMARY	41
	BIBLIOGRAPHY	43

LIST OF FIGURES

Figure 1	Atmospheric transmission from Mauna Kea, Hawai'i under two weather conditions with precipitable water vapour (PWV) levels of 0.5mm and 2.0mm. In the submm regime ($\lambda < 1\text{mm}$) the atmosphere is very opaque. Some natural atmospheric windows occur at $350\mu\text{m}$, $450\mu\text{m}$, $770\mu\text{m}$, $870\mu\text{m}$, 1.2mm and 2mm (Casey, Narayanan & Cooray, 2014). 2
Figure 2	A schematic SED for a dusty star forming galaxy at $z = 2$. The gray band represents the plausible range of SED types for a galaxy of fixed infrared luminosity $10^{12.5}\text{L}_\odot$. The black line corresponds to a representative SED for $500\text{M}_\odot\text{yr}^{-1}$ SMG. The red dashed lines correspond to model local galaxies Arp220 and Mrk231. Vertical bands represent the sensitivity of different far-infrared instruments (Casey, Narayanan & Cooray, 2014). 3
Figure 3	The left figure represents a stacked SED of 99 ALESS SMGs. The solid line represents the best fit, the gray band the range of acceptable solutions and the red and blue lines, represent the SED of M82 and Arp220 respectively. The right-hand figure shows the SED for 46 individually radio-identified ALESS SMGs with the nest fit. In this case the gray shadow also represents the acceptable solutions (Swinbank et al, 2014). 4
Figure 4	<i>Top:</i> ALESS61.1 and ALESS65.1, $870\mu\text{m}$ velocity integrated maps with $\pm 3, 5, 7, \dots \sigma$ S/N levels containing continuum+line emission. <i>Bottom:</i> continuum subtracted [CII] emission line maps with $\pm 3, 4, 5, \dots \sigma$ (Swinbank et al, 2014). 5
Figure 5	(left) Flux and (right) signal-to-noise for the LESS survey. The white square represents the size of the field while the white contour the 1.6mJy beam^{-1} noise level. the white little circles mark the position of the 126 sources detected (Weiß et al, 2009) 11
Figure 6	An example of LESS sources observed for the ALESS project. Yellow and red squares represent main and supplementary sources respectively in the catalogue. The black circle represent the primary beam FWHM. The synthesized beam is show in the left corner (Hodge et al, 2013). It is pretty much evident how a source which could look like a point source in a dish survey as in the LESS project, it could be composed by one or more sources as shown by the ALESS observations 11
Figure 7	Velocity-Averaged maps of ALESS001.1 and ALESS114.1 in right ascension (<i>x-axis</i>) and declination (<i>y-axis</i>). The red dot marks the position of the pixel with maximum flux, while the white contours correspond to the $-2, 3, 4, 5, 7, \dots \times \text{rms}$. The white circle in the left-corner is the beam size as reported in Table 1. The color bar stands for the flux intensity in μJy 15
Figure 8	Velocity-Averaged maps for ALESS001.1 to ALESS025.1 in right ascension (<i>x-axis</i>) and declination (<i>y-axis</i>). The red dot marks the position of the pixel where flux is maximum, while the white contours correspond to $-2, 3, 4, 5, 7, \dots \times \text{rms}$. The white circle in the left-corner is the beam size as reported in Table 1. The color bar stands for the flux intensity in μJy 17
Figure 9	Velocity-Averaged maps for ALESS029.1 to ALESS073.1 in right ascension (<i>x-axis</i>) and declination (<i>y-axis</i>). The red dot marks the position of the pixel where flux is maximum, while the white contours correspond to $-2, 3, 4, 5, 7, \dots \times \text{rms}$. The white circle in the left-corner is the beam size as reported in Table 1. The color bar stands for the flux intensity in μJy 18
Figure 10	Velocity-Averaged maps for ALESS076.1 to ALESS124.1 in right ascension (<i>x-axis</i>) and declination (<i>y-axis</i>). The red dot marks the position of the pixel where flux is maximum, while the white contours correspond to $-2, 3, 4, 5, 7, \dots \times \text{rms}$. The white circle in the left-corner is the beam size as reported in Table 1. The color bar stands for the flux intensity in μJy 19

- Figure 11** Circular regions used to constrained the region around the position of each source to look for the maximum flux. *left* ALESS031.1 and *right* ALESS039.1. In the case of ALESS039.1 there is a close companion which can interfere with the pixel value for the maximum flux, so both circles are large enough to contain the information of the right source and avoid possible contamination from nearby sources. the black solid circle corresponds to a radius of 0.5 arcsec while the dashed circle to a radius of 1.0 arcsec. The red dot marks the position of the maximum emission pixel in our observations. The beam size is shown in the left corner. [22](#)
- Figure 12** Likely molecules to be present in the ALESS sources plotted along the source spectrum. The red and blue vertical lines represent the most likely emission lines to be present given the redshift of the source. The green continuous line is part of the spectrum only comprising the spectral range where a line was predicted to be in. *left* ALESS006.1 in a frequency range containing spectral windows ‘0’ and ‘1’. *right* ALESS059.2 in a frequency range containing spectral windows ‘2’ and ‘3’. [24](#)
- Figure 13** *Top:* ALESS65.1 spectrum with Gaussian fitting. *Bottom:* ALESS61.1 spectrum with Gaussian fitting. In both cases the y-axis is expressed in mJy and the x-axis in GHz. Both detections satisfy a criterion of having a $\Delta\chi^2 > 20$ which corresponds to $\sigma > 4$ detection as shown in (Swinbank et al, 2012). [25](#)
- Figure 14** ALESS070.1 and ALESS122.1 spectrum. In the *x-axis* the frequency in GHz while in the *y-axis* the flux in mJy/beam. The green line represents the Gaussian fit while the dashed-yellow line the continuum. The vertical black line corresponds to the most likely molecule transition expected given the spectroscopic redshift for ALESS122.1 and the photometric redshift for ALESS070.1. In both cases CO(4 – 3) is the possible molecular transition. [28](#)
- Figure 15** ALESS070.1 and ALESS122.1 spectra in the optical. *top:* ALESS070.1 1-D (flux vs frequency) and 2-D (pixel value vs frequency) spectrum obtained with VLT/FORS2 and VLT/XSHOOTER. *bottom:* ALESS122.1 1-D (flux vs frequency) and 2-D (pixel value vs frequency) spectrum obtained with VLT/FORS2 and VLT/VIMOS. Vertical lines correspond to most likely transitions as presented by (Danielson et al, 2017). Difference between *left* and *right* images is the line position which was computed using different values of redshift. In the *left* we show the original values obtained by (Danielson et al, 2017) while in the *right* we used the redshift found using the mean frequency obtained from the fitting as reported in Table 4. [29](#)
- Figure 16** ALESS070.1 spectrum with possible molecule transition from (Spilker et al, 2014). *left:* possible transitions using the spectroscopic redshift. *right:* possible molecule transitions using the photometric redshift. Both redshifts as reported by (Danielson et al, 2017) [30](#)
- Figure 17** Different molecule transitions expected in the ALMA band4 for a few common molecules. The grey band shows the whole range in frequency covered in band4, whilst the green, purple, red and dark-grey show the four spectral windows used in our observed-data. Both, ALESS070.1 and ALESS122.1 are shown in the position expected through the line fitting obtained above (i.e redshift and observed mean frequency). A few possible transitions for CO, HCN and [CI] are shown in order to illustrate how different redshifts for a given spectral window can lead to different expected emission lines. [31](#)
- Figure 18** ALESS070.1 imaging. From left-to-right and top-to-bottom, Continuum+Line, Continuum, Line and Spitzer/IRAC images. The contours for the Continuum+Line correspond to $(-2, 3, 4, 5, 7, \dots) \times \text{rms}$ which is equal to $52.8\mu\text{Jy}$. For the Continuum, we show the $(-3, -2, 2, 3, 4, 5) \times \text{rms}$ which is equal to $56.3\mu\text{Jy}$. For the Line CO(4-3) transition we show the $(-5, -3, -2, 3, 5, 7) \times \text{rms}$ which is equal to $247\mu\text{Jy}$. For the SPITZER/IRAC counterpart (Lacy et al, 2005) we over plot the Continuum+Line contours. The red dot shows the position where the spectrum was taken and also the coordinates where the source is centred. The beam size is shown in the left-corner. The color band stands for the flux intensity. [32](#)

Figure 19	ALESS122.1 imaging. From left-to-right and top-to-bottom, Continuum+Line, Continuum, Line and Spitzer/IRAC images. The contours for the Continuum+Line correspond to $(-2, 3, 4, 5, 7, \dots) \times \text{rms}$ which is equal to $57.3\mu\text{Jy}$. For the Continuum, we show the $(-3, -2, 2, 3, 4, 5, 7) \times \text{rms}$ which is equal to $57.6\mu\text{Jy}$. For the Line CO(4-3) transition we show the $(-5, -3, -2, 5, 7, 9, 11, 13, 14) \times \text{rms}$ which is equal to $306\mu\text{Jy}$. For the SPITZER/IRAC (Lacy et al, 2005) counterpart we over plot the Continuum+Line contours. The red dot shows the position where the spectrum was taken and also the coordinates where the source is centred. The beam size is shown in the left-corner. The color band stands for the flux intensity.	33
Figure 20	Results for the CO SLED (Spectral Line Energy Distribution) of ALESS122.1. The <i>x-axis</i> corresponds to the upper J transition and the <i>y-axis</i> to the integrated intensity I_{CO} given in Jy km s^{-1} . The black dots correspond to measurements performed by (Huynh et al, 2017) for CO($1 \rightarrow 0$), (Calistro Rivera et al, 2017b) in prep. for CO($3 \rightarrow 2$) and our observation for CO($4 \rightarrow 3$). The yellow and red dots corresponds to very well known SLEDS of Arp220 (Rosenberg et al, 2015) and GN20 (Carilli et al, 2010). The first three transition for Arp220 were measured by (Greve et al, 2009). The transition CO($4 \rightarrow 3$) for GN20 was measured by (Daddi et al, 2009a). Both Arp220 and GN20 SLEDS were normalized to the CO($1-0$) transition of ALESS122.1 to properly compare.	38

LIST OF TABLES

Table 1	RMS and beam size for the ALESS sources. RMS is given in μJy while beam size in arcsec.	14
Table 2	Final sample of ALESS sources with $S/N > 4$. The coordinates in right ascension and declination are shown taking from (Hodge et al, 2013) for $870\mu\text{m}$ observations. Additionally, the spectroscopic and photometric redshift from (Danielson et al, 2017) is also presented.	16
Table 3	Transitions with fine or hyperfine structure taken from (Spilker et al, 2014). Frequencies correspond to the rest frame frequency in GHz.	23
Table 4	Fitting parameters obtained for ALESS070.1 and ALESS122.1. The redshift z corresponds to the photometric for ALESS070.1 and the spectroscopic for ALESS122.1 as reported by (Danielson et al, 2017) while the z (mean frequency) corresponds to our measurements through the CO detection.	28
Table 5	Properties computed for ALESS070.1 and ALESS122.1 in order to obtain the CO-luminosity. The units used are shown next to each quantity. Also the propagated uncertainties are presented.	36
Table 6	Properties computed for ALESS070.1 and ALESS122.1 in order to obtain the CO($1 \rightarrow 0$) equivalent luminosity and molecular mass $M(\text{H}_2)$ for ALESS070.1 and ALESS122.1	36
Table 7	Dynamical mass computed for ALESS070.1 and ALESS122.1 using the method proposed by (Solomon & Vanden Bout, 2005) to obtain M_{dyn} and (Taconni et al, 2008) $M_{\text{dyn,disk}}$. The errors are not shown because the values are just an estimation that will be finally known after measuring the half-light radius or the proper α_{CO} conversion factor for each source.	37

THEORETICAL FRAMEWORK

1.1 INTRODUCTION

During the last decades a flowering of submillimeter cosmology occurred due to the technical challenge of creating more sensitive receivers which work efficiently between radio-type and optical-like incoherent techniques. Due to the atmospheric emission and absorption sensitive submillimeter observations are allowed from only high mountains and only in specific atmosphere windows (Blain et al, 2002). However, radio interferometric observations are easier to make in comparison to the submillimeter due to the atmospheric transmission (see Figure 1). In the next sections we introduce the main concepts about submillimeter-luminous galaxies (SMGs), its main characteristics and different properties and applications. A brief description of dust, continuum and line detection for these objects is also provided. A few common molecular vibrational transitions which are present in standard SMGs are presented. We briefly discuss the characteristics of the LESS and ALESS survey which are crucial to understand our observational data and the main goal of this project.

1.2 SUBMILLIMETER-LUMINOUS GALAXIES (SMGS)

Since their discovery in the 1990's, submillimeter-galaxies have become popular objects to be studied in order to understand the star formation rates density of the universe and galaxy evolution at early epochs. Submillimeter observations are a vital component of the research for a coherent picture of the formation and evolution of galaxies, which draws on data from all wavebands where the distant Universe can be observed. SCUBA and MAMBO revealed in extragalactic Submillimeter/Millimeter (submm/mm) surveys a new population of very luminous-high redshift sources (Blain et al, 2002). This population known as SMGs, as a whole is responsible of a significant fraction of the energy generated by all galaxies over the history of the Universe (Blain et al, 1999b). Their particular characteristics, make them special objects of interest to study the early universe, the star formation rates and the evolution of galaxies at high redshift. Models which try to explain the redshift distribution and the observed abundance of SMGs have problems which motivates to study them in detail (Blain et al, 2002). On the other hand, these sources are thought to be a class of ultraluminous infrared galaxies (ULIRGs) which are known to show bolometric luminosities (integrated over all wavelengths at which dust emission dominates the spectral energy distribution (SED) (Blain et al, 2002)) $L_{\text{bol}} > 10 \times 10^{12} L_{\odot}$ at redshifts $z \sim 2 - 3$ (Decarli et al, 2016; Hayward et al, 2011). ULIRGs at low-redshift seem to be late-state merger-induced starbursts (often with an active galactic nuclei (AGN) significant contribution), then it is widely supposed that SMGs are also merger-induced starbursts (Lonsdale et al, 2006) (Sanders & Mirabel, 1996). SMGs are powered primarily by star formation rather than AGN. This is due to the rapid increase in gas fraction and SFRs of galaxies at a fixed galaxy mass. Also the fact that High redshift galaxies have a huge gas supply onto them (Hayward et al, 2011). Thus, at

$z \sim 2 - 3$ a normal star-forming galaxy can reach ULIRGs luminosities.

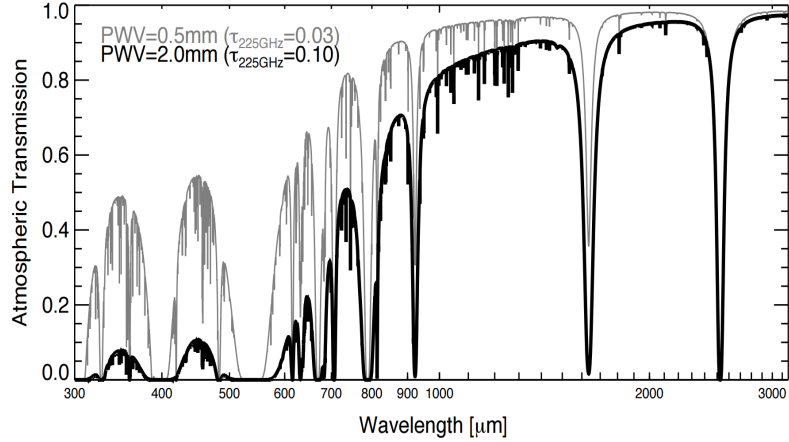


Figure 1: Atmospheric transmission from Mauna Kea, Hawai'i under two weather conditions with precipitable water vapour (PWV) levels of 0.5mm and 2.0mm. In the submm regime ($\lambda < 1\text{mm}$) the atmosphere is very opaque. Some natural atmospheric windows occur at $350\mu\text{m}$, $450\mu\text{m}$, $770\mu\text{m}$, $870\mu\text{m}$, 1.2mm and 2mm (Casey, Narayanan & Cooray, 2014).

If we want to study this population of galaxies, we need to match them with their different counterparts in other bands. However, matching submillimeter galaxies to radio counterparts is challenging, because in comparison to optically-bright galaxies, radio sources are much more rare and it is not common to have more than one visible within one submillimeter beam. Radio bright makes reference to a radio source with $S_{1.4} \gtrsim 50\text{--Jy}$ (Casey, Narayanan & Cooray, 2014)). The source can be quickly identified in different wavelengths, commonly near-infrared and optics to do spectroscopy, once the position is well known through radio detection. This leads to positions and redshifts which can be used to physically characterize the sources. Different characteristics important to unveil the hidden physics of SMGs as the spectral energy distribution, line emission, continuum emission from dust and others are presented in next sub-sections.

1.3 SED

Thermal continuum emission from dust grains, the solid phase of the interstellar medium (ISM) and line emission from atomic and molecular in the interstellar gas transitions constitute the major processes which produce submillimeter radiation in galaxies. Line observations provide a scenario suitable to study the physical and chemical conditions of the ISM as the kinematics, metallicity and excitation conditions. Also to obtain very accurate spectroscopic redshifts. Dust emission paves the way to study SMGs spectral energy distributions because it is dominated by thermal emission produced by dust grains, heated by energy absorbed from stars and AGN. Submillimeter observations can be complemented with UV-Optical observations in order to obtain new information which is not available in the submm bands as unobscured star formation and AGN emission (Blain et al, 2002). In Figure 2, a representative SED for a SMG is shown. The black line represents an SMG with SFR of $500\text{M}_\odot\text{yr}^{-1}$ while the red lines represent modelled SEDs of very well studied sources as Arp220 and Mrk231. This SED have peak wavelengths from $70 - 130\mu\text{m}$ which corresponds to temperatures of $30 - 58\text{K}$. The vertical lines shows the sensitivity of different detector in this wavelength range which are commonly used to obtain the flux

density at a given frequency to lately fit the plausible SED.

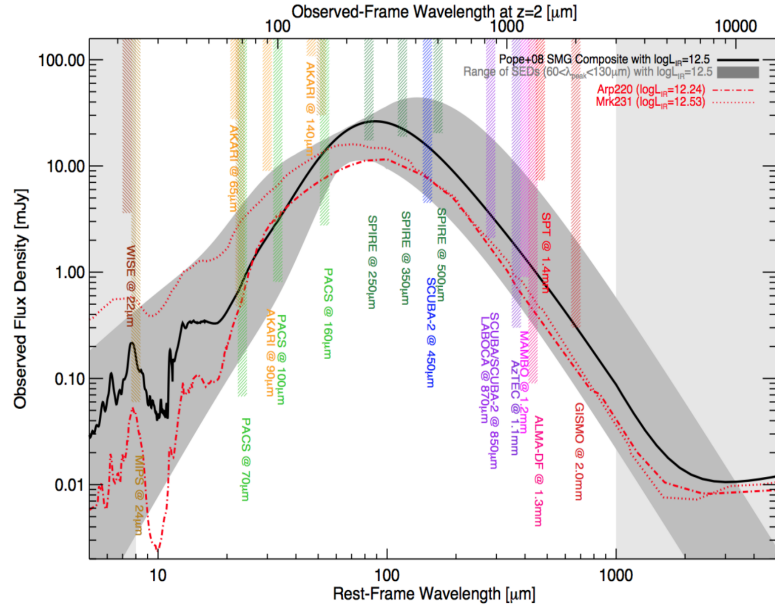


Figure 2: A schematic SED for a dusty star forming galaxy at $z = 2$. The gray band represents the plausible range of SED types for a galaxy of fixed infrared luminosity $10^{12.5}L_\odot$. The black line corresponds to a representative SED for $500M_\odot \text{yr}^{-1}$ SMG. The red dashed lines correspond to model local galaxies Arp220 and Mrk231. Vertical bands represent the sensitivity of different far-infrared instruments (Casey, Narayanan & Cooray, 2014).

In typical spiral galaxies, the dust is found to be extended on the same scale as the stellar disk, then the emission is associated with gas rich star-forming regions distributed throughout the galaxy where dust is heated by the hot, young OB stars. Moreover, in intermediate luminosity galaxies, the star forming places where most of the luminosity comes from is a deeply dust-enshrouded overlap region of the ISM, providing strong evidence that most of its energy is produced by star formation rather than AGN. In the case of ULIRGs, the great majority of the dust emission arises in a much smaller, sub-kpc region within a merging system of galaxies, so a significant fraction could be derived from an AGN surrounded by a very great column density of gas and dust (Blain et al, 2002). As an example, in Figure 3 the SED for stacked ALESS sources made by (Swinbank et al, 2014) is provided. The left figure for 99 sources with M82 and Arp220 for comparison, and the right for 46 with radio counterparts. The shaded gray band shows the acceptable solutions. The images of the stacks of *Hershel* / PACS + SPIRE (70 – 500 μm), ALMA 870 μm and VLA (1.4GHz) are shown. We can see that radio detected composite has more flux at shorter wavelengths (Swinbank et al, 2014; Iglesias-Groth et al, 2017).

Additionally, the SED of SMGs has a Rayleigh-Jeans tail that produces a negative k-correction in the submillimeter regime, yielding a near constant flux density-luminosity dependence with redshift over the range $z \sim 1 - 6$ (Blain et al, 2002). Moreover, the volume density appears to subsequently decline above $z \gtrsim 3$, which is not a result of a reduction in the apparent flux density in the submillimeter but a real reduction in the volume density of SMGs (Wardlow et al, 2011). Generally in submillimeter surveys sources lack of counterparts in the radio or mid-infrared around 30% – 50%, representing an unidentified tail of the high redshift SMGs (Biggs et al, 2011; Lindner et al, 2011), but can be solved using interferometers instead of single dishes. The whole population of SMGs requires precise location of the submillimeter emission using interferometers

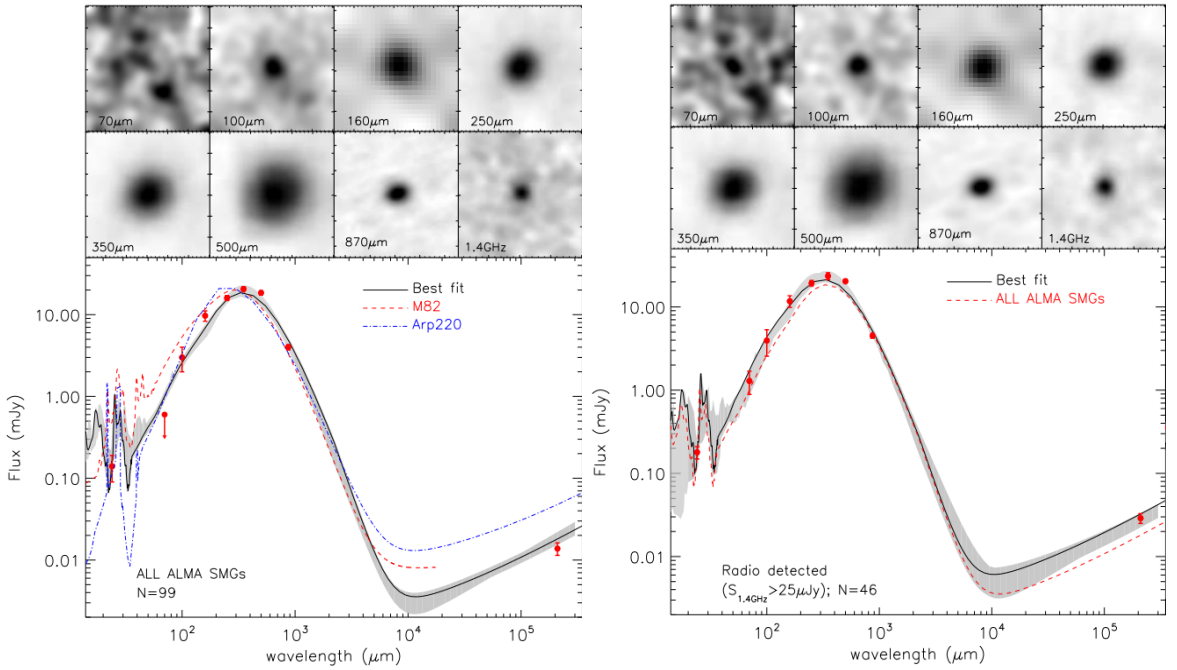


Figure 3: The left figure represents a stacked SED of 99 ALESS SMGs. The solid line represents the best fit, the gray band the range of acceptable solutions and the red and blue lines, represent the SED of M82 and Arp220 respectively. The right-hand figure shows the SED for 46 individually radio-identified ALESS SMGs with the nest fit. In this case the gray shadow also represents the acceptable solutions (Swinbank et al, 2014).

and redshift distributions. If we want to constrain with high accuracy the theoretical models, then the bolometric luminosities, cold molecular gas dynamics, gas mass, and contribution to the star forming density must be studied in detail (Swinbank et al, 2014).

1.3.1 Continuum Emission From Dust

Dust emission is a thermal process characterized by a modified black body spectrum. Depending on the spectrum intensity of the interstellar radiation field, its size and optical properties, the dust grains can be heated to temperatures between 20 – 200K (Blain et al, 2002). Very small grains can be heated by absorbing hard-UV photons, leading to high dust temperatures if they are close to a powerful source of radiation or low temperature in opaque regions of the ISM where they are shielded from the radiation field. The cosmic microwave background radiation can also boost the dust and gas temperatures in high redshift galaxies (da Cunha et al, 2013), enhancing the dust continuum and CO line emission. Dust continuum emission is of particular interest in the study of star formation in high redshift galaxies because as the dust spectral energy distribution shifts to higher and higher redshifts, we observe closer and closer to the peak of the dust emissivity at submillimeter wavelengths (Decarli et al, 2014).

In any galaxy, a gradient of dust temperature shows the different nature and environment where each grain lives in. Most of dust temperatures were not available in the high Universe pre-Hershel due to the lack of FIR SED measurements to constrain the dust temperature directly. However, even if the temperature is not well constrained, a flux density measurement in the Rayleigh-Jeans tail which corresponds to a optically-thin regions can provide a decent dust

mass estimator (Casey, Narayanan & Cooray, 2014). This method can be combined with the gas-to-dust ratio to infer the H₂ total mass in the ISM, which is important in order to describe the star formation and the duration of the starburst (Swinbank et al, 2014).

1.3.2 Line Emission

Photodissociation regions and molecular clouds can be studied using emission from molecular rotation and atomic fine-structure transition lines. Some lines as CS, HCN and HCO+ are excited only in high-density gas, while others including CO trace more typically the cold ISM (Blain et al, 2002). CO-line observations allow us to confirm an absolute identification, by tying together an optical and submm redshift at the position of the galaxy. On the other hand, the predominant fine-structure lines studied correspond to ionized carbon, nitrogen and oxygen, with particular emphasis on [CII] ionized fine-structure line (Swinbank et al, 2014). The last, is though to be produced by collisions with neutral hydrogen, or with free electrons and protons when the electron density is high enough. As an example in Figure 4 for ALESS61.1 and ALESS65.1, the continuum+line emission is shown in the top panel with $\pm 3, 5, 7\dots\sigma$ S/N levels, whilst in the bottom panel just the [CII]-line with $\pm 3, 4, 5\dots\sigma$. This is a good example of how a line detection in a SMG galaxy looks like after calibration, cleaning and subtraction processes.

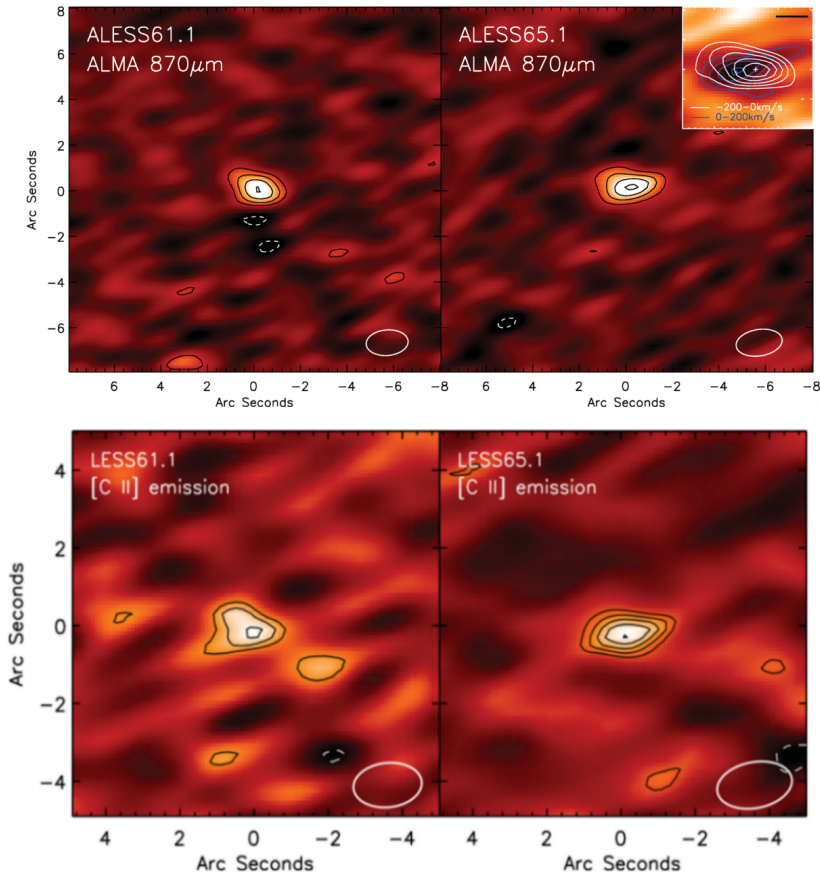


Figure 4: Top: ALESS61.1 and ALESS65.1, 870 μ m velocity integrated maps with $\pm 3, 5, 7\dots\sigma$ S/N levels containing continuum+line emission. Bottom: continuum subtracted [CII] emission line maps with $\pm 3, 4, 5\dots\sigma$ (Swinbank et al, 2014).

1.4 MOLECULE TRANSITIONS

Physical properties of the ISM can be studied in high redshift galaxies making use of the strength of atomic lines and molecule transitions' relative strength to far-infrared luminosities (Swinbank et al, 2014). A unique insight in molecular line observations, provide constrains on the kinematics of the galaxy, dynamical and gas masses estimates, gas luminosities among others (Huynh et al, 2017; Ginolfi et al, 2017). Studying molecular lines has set one of the main ways during the last decade to know more about the early Universe. The evolution of galaxies is strongly linked to the molecular interstellar medium providing the first evidence about the location and mass of molecular clouds during the epoch of galaxy formation (Solomon & Vanden Bout, 2005). We will mainly focus on CO-emission because it will help to understand deeply the results of this research project. However, we also present some other important molecule transition in next sections because they pave the way to really understand how to tackle down the physics of SMGs and could be very useful for future works and observations at different redshift and with different emission lines.

1.4.1 *CO emission*

A few decades ago, detecting CO emission for sources with $z \gtrsim 0.3$ (not local galaxies but extragalactic) was not possible because of the low sensitivity of telescopes and arrays at millimeter wavelengths. Nevertheless, the increase in sensitivity and additionally suitable scenario as large masses of molecular gas, a negative K-correction for CO-emission, gravitational lensing of many sources and strong far-infrared emission (FIR) facilitated CO and other molecule detections. There exists three methods to find SMGs with possible CO emission (Solomon & Vanden Bout, 2005): the first employs searching for bright optical high redshift quasars, the second one includes identifying highly luminous infrared galaxies from blank field observations with submillimeter-wave bolometers and the last one involves the strategy to search for infrared luminous radio galaxies. Important redshift measurements are required in order to properly characterize CO emission in distant galaxies. CO detections helps to answers questions as: What is the amount of mass in the form of molecular gas and how does it relate to the dynamical mass in the system? What is the distribution of the gas in SMGs? Are they highly concentrated or extended? What is the star formation lifetime in this sources? What is the final evolutionary state of the SMGs?. CO rotational transition is one of the most accessible tracers of cold molecular mass (Carilli et al, 2013), and specially CO($1 \rightarrow 0$) because it is less affected by excitation conditions of the gas providing a robust estimate of overall molecular gas content, becoming the broadest tracer of the dynamics in the system (Huynh et al, 2017). In sub-section 1.4.1.1 and sub-section 1.4.1.2 we address a brief description about the basic relations between the CO luminosity and other molecular luminosities and its relation to the amount of gas (i.e molecular gas H₂) and the connexion with the dynamical mass of the system which will be used to obtain the main physical properties of our sources. The rest-frame frequencies for the most common CO transitions observed in SMGs are shown in Table 3.

1.4.1.1 *CO Luminosity*

First of all, the main goal when observing a molecule transition is to use the line properties to infer the physics of the environment where the gas lives in, to describe the general properties of

a source. There is a direct connexion between the physics hidden in the source and the emission line we observe. One of the most crucial parameters which must be well known before addressing this problem, to properly identify a given line is the redshift. All our quantities and definitions will depend on redshift or cosmological distance, then a slightly wrong measurement will lead to wrong characterization of the emission line and also to incorrect values in the derived properties for the SMGs. The cosmology assumed throughout this work corresponds to a Universe with $\Omega_m = 0.3$, $\Omega_\Lambda = 0.7$ and $H_0 = 70 \text{ km s}^{-1} \text{ Mpc}^{-1}$, where Ω_m and Ω_Λ correspond to the matter and dark energy density coefficients and H_0 to the Hubble constant respectively.

There are different ways to express the CO luminosity depending on what parameters you can measure according to the observational data. Using the energy conservation theorem, the monochromatic luminosity, observed flux density and luminosity distance we can obtain a relation which follows $v_{\text{res}} L(v_{\text{res}}) = 4\pi D_L^2 v_{\text{obs}} S(v_{\text{obs}})$ (Solomon & Vanden Bout, 2005) yielding to,

$$L'_{\text{CO}} = 1.04 \times 10^{-3} S_{\text{CO}} \Delta v v_{\text{res}} (1+z)^{-1} D_L^2 \quad (1.1)$$

In order to obtain the CO luminosity L'_{CO} in L_\odot , the velocity integrated flux $S_{\text{CO}} \Delta v$ must be given in Jy km s^{-1} , the rest frame frequency $v_{\text{res}} = v_{\text{obs}}(1+z)$ in GHz and the luminosity distance D_L in Mpc. Sometimes, this luminosity is expressed in units of $\text{K km s}^{-1} \text{ pc}^2$, as the product of the velocity integrated source brightness temperature ($T_b \Delta v$) and the source area ($\Omega_s D_A^2$) (Solomon & Vanden Bout, 2005), where Ω_s is the solid angle subtended by the source and D_A is the angular size distance. Hence and taking into account that the line luminosity can be written as $L'_{\text{CO}} = T_b \Delta v \Omega_s D_A^2 = \Omega_{s*b} D_L^2 I_{\text{CO}} (1+z)^{-3}$, then we get,

$$L'_{\text{CO}} = 23.5 \Omega_{s*b} D_L^2 I_{\text{CO}} (1+z)^{-3} \quad (1.2)$$

Here Ω_{s*b} is the solid angle of the source convolved with the telescope beam in arcsec^2 , I_{CO} the integrated line intensity is given in K km s^{-1} and D_L in Mpc. Equation 1.2 depends on the source size, therefore, to include a more general case for a source of any size we can rewrite this as,

$$L'_{\text{CO}} = 3.25 \times 10^7 S_{\text{CO}} \Delta v v_{\text{obs}}^{-2} D_L^2 (1+z)^{-3} \quad (1.3)$$

Equation 1.3 is the final form for the CO-luminosity and the most general one, which will be adopted through this work following (Decarli et al, 2016; Casey, Narayanan & Cooray, 2014). As can be seen from Equation 1.2 and Equation 1.3 for a fixed line luminosity and observing frequency, the observed integrated line intensity and the integrated flux do not scale as D_L^{-2} but as $(1+z)^3 D_L^{-2}$ which reflects the negative K-correction which benefits the millimeter atmospheric window to observe CO (Solomon & Vanden Bout, 2005).

1.4.1.2 Molecular mass H_2

Once we have defined the explicit form for the CO-luminosity, we can then find a relation to derive the molecular mass i.e. m_{H_2} . Interstellar molecular clouds which consist almost entirely of molecular hydrogen are traced by the CO rotational transitions. Rather than atomic hydrogen, molecular hydrogen is the main component of molecular clouds with a density $n > 100 \text{ cm}^{-3}$ due to a balance between formation on dust and self-shielding of H_2 from photodissociation by

the interstellar radiation field (Solomon & Vanden Bout, 2005). Knowing more about the physics of molecular clouds is important because this is a critical component in the evolution of galaxies which affects directly the star formation. First stars are expected to form from HI with only traces of H₂ available to provide cooling. However, the observed SMGs show a huge IR luminosity clearly emitted by interstellar dust, then it is expected that all dense, dusty clouds to be molecular. H₂ requires a special scenario as high temperature, to produce the vibration-rotational lines and also it has strongly forbidden rotational transitions. This is why we need to draw on the CO emission, because it is very stable and the most abundant after molecular hydrogen (Walter et al, 2016). Additionally, CO molecule has a weak dipole which means that CO rotational levels are excited and thermalized by collisions with H₂ at relatively low molecular hydrogen densities (Solomon & Vanden Bout, 2005). In order to guarantee strong CO emission the interstellar medium must have a given effective density. For example has to be $n(H_2) \approx 300\text{cm}^{-3}$ for a $J = (1 \rightarrow 0)$ transition and almost $n(H_2) \approx 3000\text{cm}^{-3}$ for a $J = (4 \rightarrow 3)$ or $J = (5 \rightarrow 4)$ transition, where the highest transitions need also a minimum kinetic temperature for collisional excitation (Solomon & Vanden Bout, 2005).

On the other hand, SMGs contain large quantities of dust and molecular gas which indicates not only ongoing star formation but previous enrichment from previous star formation. This, leads to a high metallicity and an extended region of enriched interstellar matter which can be studied through the luminosity of carbon monoxide. The H₂ mass-to-CO luminosity is expressed in (Casey, Narayanan & Cooray, 2014; Solomon & Vanden Bout, 2005) as,

$$M(H_2) = \alpha L'_{CO} \quad (1.4)$$

where we must be cautious because $M(H_2)$ contains also the Helium-mass, so it represents the total gas mass in the molecular clouds and not only the molecular one. The α parameter represents a conversion factor that encloses all the physics related to the H₂ number density and the intrinsic (rest-frame) brightness temperature and it is usually written in units of $M_\odot(K\text{ km s}^{-1}\text{ pc}^2)^{-1}$. In the literature different values are found for α because it depends on the region CO is located in, where exactly the emission is produced at, the physical conditions of the gas among others (Casey, Narayanan & Cooray, 2014). Different values from $\alpha = 4.6M_\odot(K\text{ km s}^{-1}\text{ pc}^2)^{-1}$ for the milky way or $\alpha = 0.8M_\odot(K\text{ km s}^{-1}\text{ pc}^2)^{-1}$ for SMGs are used without a real consensus. Then, we will left the conversion factor as a free choice parameter along this work.

In addition, there is a relation between CO line emission and a medium bound by a total potential of the galactic center, containing a mass M_{dyn} , consisting of stars given in (Solomon & Vanden Bout, 2005) by,

$$M_{dyn}M_{gas} = (\alpha L'_{CO})^2 \quad (1.5)$$

Additionally to this method, if we use the isotropic virial estimator as presented by (e.g., Spitzer 1987, we can also obtain the dynamical mass in terms of the half-light radius $R_{1/2}$ and the one-dimensional velocity dispersion σ^2 which encapsulates the FWHM integrated line width as given by,

$$M_{dyn,vir}(R \leq R_{1/2}) = \frac{5\sigma^2 R_{1/2}}{G} = \frac{5}{2.35^2} \frac{\Delta_{vFWHM}^2 R_{1/2}}{G} \quad (1.6)$$

If we apply an average of the virial estimator and global rotating disk estimator corrected by inclination in velocity and mass we get the next expression reported by (Tacconi et al, 2008),

$$M_{\text{dyn,disk}}(R \leq R_{1/2}) \approx 6 \times 10^4 \Delta_{\text{vFWHM}}^2 (\text{km s}^{-1}) R_{1/2} (\text{kpc}) M_{\odot} \quad (1.7)$$

Multiplying by a factor of two the last expression, we can obtain the total dynamical mass just as an extrapolation for the star forming regions in a source (Tacconi et al, 2008).

To give an indicator of the star formation rate per solar mass of molecular gas, we can use the CO-luminosity and far-infrared luminosity ratio ($L_{\text{FIR}}/L'_{\text{CO}}$). This is often taken as a measure of the star formation efficiency. This can be explained by the fact that in SMGs, the star formation efficiency is higher than in normal spiral galaxies due to the high fraction of molecular gas traced not only by CO but by HCN and other molecules, marking a well-established trend where star formation efficiency increases with FIR luminosity (Solomon & Vanden Bout, 2005).

1.4.2 *HCN, [CI] and [CII] emission*

In this work we focus on CO-emission, however it is not the only molecule used to trace the molecular gas reservoir in a galaxy. There are a bunch of molecule and atomic transitions used, but we will only briefly described three of them which are more likely to be found in the SMGs. The molecule is the hydrogen cyanide (HCN) and the atomic carbon ([CI]) and ionized carbon ([CII]). These molecule transitions can be several times fainter than CO (Carilli et al, 2016) but could trace different regions of the molecular clouds, letting us know different physics of the interstellar medium of SMGs depending on the place we observe the transition. In Table 3, the expected rest-frame frequency for this molecule transitions are shown.

Hydrogen cyanide is known to trace very well dense molecular gas regions where the molecular hydrogen density is $n(\text{H}_2) > 3 \times 10^4 \text{ cm}^{-3}$. This regions are generally associated with the star-forming cores of giant molecular clouds, instead of lower density regions as the envelope where CO is found. Hence, HCN line luminosity traces better the star formation than CO, while CO is a better tracer of the total molecular mass (Swinbank et al, 2012; Solomon & Vanden Bout, 2005). Those galaxies which seems to be luminous IR sources in general show a huge HCN line luminosity, making the ratio $L'_{\text{HCN}}/L'_{\text{CO}}$ high, indicating the large amount of dense gas present in comparison to the total amount of molecular gas. It is well known that the ratio of IR luminosity and HCN luminosity is the same for *ULIRGs* and lower luminosity galaxies as the normal spiral galaxies, indicating that this objects are powered basically by star formation. This fact, ratifies the HCN line as a good estimator of mass in actively star-forming cloud cores (Gao & Solomon, 2004; Solomon, Downes & Radford, 1992b).

Besides HCN-emission, we have atomic carbon emission [CI] which has been found to be closely associated to CO-emission in the Milky Way and nearby galaxies, tracing really well the surface of molecular clouds (Popping et al, 2017). The [CI](${}^3\text{P}_1 \rightarrow {}^3\text{P}_0$) transition at 492.160 GHz and [CI](${}^3\text{P}_2 \rightarrow {}^3\text{P}_1$) at 809.342 GHz happen at roughly the same critical density for excitation of CO($1 \rightarrow 0$), this suggests that CO and [CI] emission originates in the same volume (Solomon & Vanden Bout, 2005). This presents a scenario where we can test the emission region independently of CO to infer [CI] excitation, physical conditions of the environment and amount of

mass in the reservoir. There exists relations to obtain the mass from the [CI] excitation temperature where one only needs to know the ratio of line luminosities for transitions ($2 \rightarrow 1$) and ($1 \rightarrow 0$).

On the other hand, an important coolant for the photodissociation regions of molecular clouds predicted by models is the ionized carbon [CII] fine-structure transition (${}^2\text{P}_{3/2} \rightarrow {}^2\text{P}_{1/2}$), even more than CO, [CI] or any other atomic fine-structure line (Swinbank et al, 2012; Solomon & Vanden Bout, 2005). With [CII] one can trace the warm and dense photodissociation region which forms on the uv-illuminated surface of molecular clouds obtaining the gas content and the extent of gas reservoir (Swinbank et al, 2012). Also a significant flux of HII which represents the cool diffuse interstellar gas can be found. ALMA sensitivity improved the detection of this line in high redshift galaxies and also open the possibility to resolve star-formation and map the morphology (Combes et al, 2013; Hodge et al, 2016). All this molecular transitions discussed are essential to understand the different mechanisms involved in the assembling of galaxies and star formation in the early universe, providing better measurements to help us understand deeply the morphology, kinematics and gas density estimates in SMGs.

1.5 ALESS SURVEY

The *ALESS*-survey was conceived as an extension of the *LESS*-survey in order to improve the quality of the data and better constrain the physical properties of SMGs. The LABOCA *Extended Chandra Deep Field South* (ECDFS) Submillimeter Survey (LESS) is an extragalactic survey using the LABOCA Camera on the MPIfR/ESO/OSO-owned 12-m APEX Telescope covering a field of $0.5^\circ \times 0.5^\circ$ at RA $03^\text{h} 32^\text{m} 28.0^\text{s}$ and DEC $-27^\circ 48' 30.0''$ of 126 sources. These observations were carried out between May 2007 and 2008 November under optimal weather conditions with PWV of 0.5mm and at $870\mu\text{m}$ (345GHz). At this frequency the passband has a FWHM of $150\mu\text{m}$ (60GHz) and an angular resolution of each beam of $19.2''$ FWHM (Weiβ et al, 2009). Excluding overhead, the survey was done during 200h of on-sky-integrations with extremely uniform noise (on average $\text{rms} = 1.2\text{mJy beam}^{-1}$) (Biggs et al, 2011). The ECDFS is a unique field in the southern hemisphere which mixes a good combination of area, depth and an extensive multiwavelength coverage (Karim et al, 2013) that covers from x-rays, optical, near, mid and far infrared to radio regimes. In Figure 5, we have the flux (left) and signal-to-noise maps (right) of the LESS survey as shown in (Weiβ et al, 2009). The white contour corresponds to the 1.6mJy beam^{-1} noise level used to defined the field size, the square represents the $0.5^\circ \times 0.5^\circ$ field and the white circles the position of every source in the survey.

Although, the LESS survey was an improvement as for the detection of SMGs, several problems needed to be fixed up. The limitation of single-dish submillimeter surveys as LESS is the poor angular resolution which leads to issues in the interpretation of data. This causes uncertainties in source position, hiding multiple sources into one, biasing the sample against faintest/highest redshifts SMGs (Hodge et al, 2013). Multiple single dish submillimeter sources lead to a misidentification in 30% of the cases as shown by (Karim et al, 2013; Simpson et al, 2015b). Therefore, in order to overcome this problems the ALESS project was created using the new capabilities of ALMA. The main goals focused on obtaining an unbiased catalogue to derive accurate physical parameters which describe this population of galaxies as mass, dynamics of the gas, star formation rates and others (Danielson et al, 2017). As stated before, this uses the interferometric power of ALMA to make a complete and unbiased view of SMGs (Hodge et al, 2013), and provide a large, flux-limited sample of submillimeter sources over a wide area in the ECDFS (Karim et

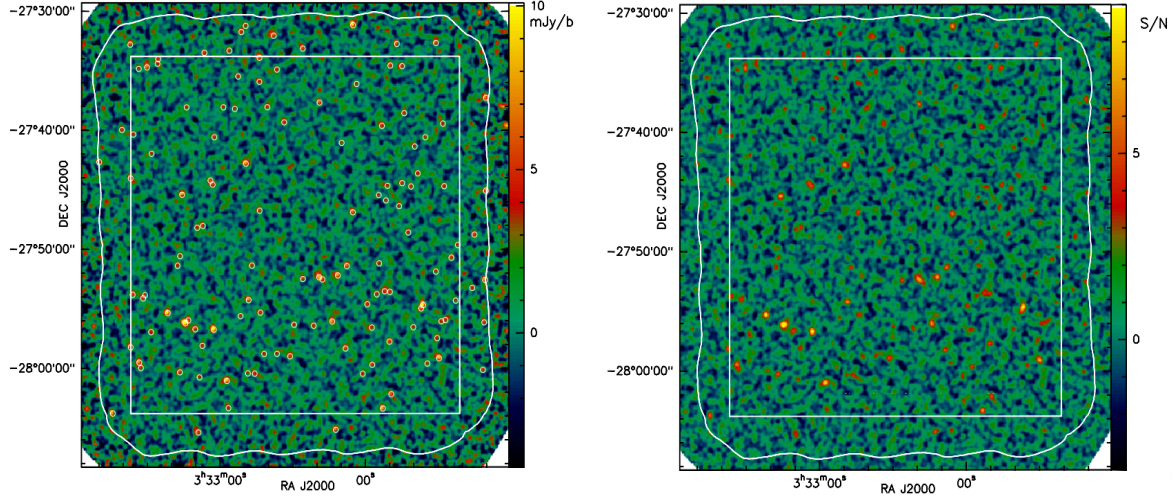


Figure 5: (left) Flux and (right) signal-to-noise for the LESS survey. The white square represents the size of the field while the white contour the 1.6mJy beam^{-1} noise level. the white little circles mark the position of the 126 sources detected (Weiβ et al, 2009)

al, 2013). Thanks to ALMA capabilities, it has been possible to achieve angular resolution and sensitivity necessary to identify counterparts of submillimeter galaxies to $\lesssim 0.3''$ accuracy without recourse to statistical associations at other wavelengths (Danielson et al, 2017) and to carry on observations of large samples (Hodge et al, 2013). ALESS collected information at the same effective frequency of the LESS survey but with a three times better r_{rms} of $\approx 0.4\text{mJy beam}^{-1}$ and a 200 times smaller beam size ($1.5''$) avoiding the source blending problem (Decarli et al, 2014). Not all the original sources detected by (Weiβ et al, 2009) were targeted, but 122 out of 126 in the ALMA Cycle-0 at $870\mu\text{m}$ (344GHz - Band7) between 2011 October 18th and November 3rd with the array in compact configuration (largest baseline of 125m) and 15 antennas (Hodge et al, 2013). The position of the ALESS survey correspond to the $870\mu\text{m}$, so they can slightly vary at any other frequency because the emission peak flux could come from a different location in the SMG at the given frequency.

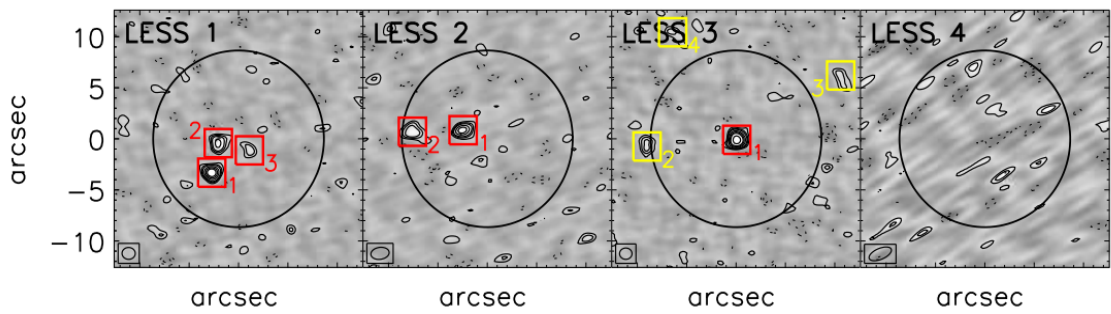


Figure 6: An example of LESS sources observed for the ALESS project. Yellow and red squares represent main and supplementary sources respectively in the catalogue. The black circle represent the primary beam FWHM. The synthesized beam is show in the left corner (Hodge et al, 2013). It is pretty much evident how a source which could look like a point source in a dish survey as in the LESS project, it could be composed by one or more sources as shown by the ALESS observations

As can be seen in Figure 6 (just a small sample taken from (Hodge et al, 2013)), LESS sources LESS1, LESS2, LESS3 and LESS4, which at first glance with APEX look like one single galaxy, here

it can contain multiple sources pretty close to each other as is the case for LESS1. The black circle represents the primary beam FWHM while the red and yellow squares the main candidates and supplementary ones added to the survey. As can be seen and as stated before, ALMA avoids the blending problem and enhances the sensitivity and angular resolution putting up a perfect scenario to study this galaxy population and adding valuable new sources.

Since SMGs are thought to be linked to both QSO activity and the formation of massive ellipticals in the local universe, it is necessary to guarantee well measured spectroscopic redshifts to constrain the SED, so the templates used in the models of galaxy formation and evolution for this population will be more accurate (Hodge et al, 2013; Danielson et al, 2017). The LESS and ALESS surveys have led to different results as a serendipitous identification of [CII] emission in SMGs at $z \approx 4.4$ (Swinbank et al, 2012), optical and near infrared properties, photometric redshifts distribution and stellar masses studied by (Simpson et al, 2014), x-ray properties and AGN fraction of ALMA SMGs (Wang et al, 2013), a source catalogue and multiplicity (Hodge et al, 2013) and high resolution submillimeter counts (Karim et al, 2013), far-infrared correlation of SMGs (Thomson et al, 2014), far-infrared/submillimeter properties (Swinbank et al, 2014), Cold molecular gas (CO) follow-up (Huynh et al, 2017) and spectroscopic redshifts by (Danielson et al, 2017). All this have led to a better description of SMGs which is a totally brand new field in radio astronomy and it has evolved rapidly in the last decades thanks to the modern instruments.

Recently, a new and very important additional survey called *z*LESS-survey has targeted statistically-identified radio/mid-infrared counterparts to the submillimeter sources identified in (Biggs et al, 2011), as well as a large number of other galaxy populations in the same regions. However, according to (Hodge et al, 2013), there is an offset present in the coordinates because the sources need to be deblended. They corrected their coordinates to the ALESS-identified sources. The main goal is to provide an unbiased catalogue of SMGs to derive molecular gas masses, as well as measure spatially resolved dynamics of the gas and stars in order to identify the triggering mechanisms that cause the burst of star formation (Danielson et al, 2017). They wanted to get redshifts for all the sources but only obtained around 50% of them because these galaxies can be very faint in the optical, hence, obtaining their spectra is not an easy task. This shows why it is in some way important to perform blind submillimeter scans for emission lines in order to obtain redshifts, because most of the time we can not obtain them through optical observations.

This work was carried out with ALMA observations of ALESS sources in the Band4. The main goal is to find any emission line in a sub-sample of ALESS sources and characterize the emission to subsequently compute different physical properties as line luminosity and molecular mass. In Chapter 2 we present the characterization of the observational data, our final sample of galaxies and imaging. In Chapter 3 the spectrum extraction process and line fitting is presented. In Chapter 5 and Chapter ?? the physical properties derived for the final sample and conclusions are presented respectively.

OBSERVATIONAL DATA: FINAL SAMPLE

2.1 INTRODUCTION

In this chapter we present the observational data used to achieve the main goals of this research project. The process of calibration using CASA and the criteria used to select the final sample to work with, are briefly explained. The observations were part of an *ALMA* project carried out by Dr. Elisabete da Cunha from the Australian National University in order to study the dust continuum in sub-millimetre galaxies. However, as we get 3D-information when we observe in radio we decided to use the available data to study the spectral emission lines in these sources if present. The procedure to obtain the our sample and the imaging process of each source are presented in order to make a point on which are the targets we will work with in next sections.

2.2 SAMPLE OF GALAXIES AND CALIBRATION

The observational data we used to develop this project is part of a project "*A complete census of dust in sub-millimetre galaxies*" in charge of the P.I. Dr. Elisabete da Cunha from the Australian National University. The project was part of the *ALMA*-Cycle 3 and a sample of 69 sources were observed from 01-Jan-2016/02 : 04 : 34.2 to 01-Jan-2016/03 : 10 : 19.6 in the *Band-4* (C36-1 configuration) in order to properly study the continuum emission of dust in ALESS sources. The proposed *rms* was 60 μ JY in a 7.5 GHz bandwidth and a beam size of 2.3 arcsec. In order to calibrate the data, a flux calibrator (*J0334 – 4008*) and phase calibrator (*J0348 – 279*) were also observed. The first one at the beginning of the night, and the second one right away the flux calibrator and after every twelve sources because the phase can vary very rapidly during the observation lowering down the resolution. In average, every source was observed for around 40 seconds. Sources were clearly detected in 51 out of the 69 targets with an average *rms* of 52.6 μ Jy/beam and a beam size within the 10% proposed. The values listed in [Table 1](#) correspond to the final beam size and *rms* of every source after correcting the data i.e after the calibration process. The calibration process was carried out using an automated pipeline (CASA 4.5.1 –pipeline) in order to correct for the flux and frequency phase dependency. In this process the packaged calibration and flagging tables are applied instead of being regenerated. The entire calibration procedure results in the final measurement sets ready for imaging. Although this project was carried out in order to study the dust properties via the continuum emission, we will take advantage of the fact that when you observe in radio you get 3D-data for free, so we will search for any kind of emission line present in these sources to determine extra properties which are important to describe this SMGs population.

Table 1: *RMS* and beam size for the ALESS sources. *RMS* is given in μJy while beam size in arcsec.

Name	RMS [μJy]	Beam size ([arcsec][arcsec])	Name	RMS [μJy]	Beam size ([arcsec][arcsec])	Name	RMS [μJy]	Beam size ([arcsec][arcsec])
ALESS001.1	50.00	2.37×2.24	ALESS041.1	52.90	2.41×2.26	ALESS080.1	53.30	2.46×2.27
ALESS002.1	50.70	2.38×2.25	ALESS043.1	51.10	2.41×2.26	ALESS082.1	52.60	2.47×2.27
ALESS003.1	50.80	2.38×2.25	ALESS045.1	51.50	2.42×2.27	ALESS083.4	51.40	2.47×2.28
ALESS005.1	51.60	2.38×2.26	ALESS049.1	54.30	2.42×2.26	ALESS084.1	51.30	2.47×2.27
ALESS006.1	49.70	2.38×2.25	ALESS051.1	50.30	2.42×2.27	ALESS087.1	52.50	2.47×2.27
ALESS007.1	48.40	2.38×2.25	ALESS055.1	52.70	2.42×2.27	ALESS088.1	54.80	2.48×2.28
ALESS009.1	52.30	2.37×2.25	ALESS057.1	52.90	2.43×2.27	ALESS092.2	54.40	2.47×2.26
ALESS010.1	51.70	2.38×2.26	ALESS059.2	50.50	2.43×2.27	ALESS094.1	53.10	2.47×2.27
ALESS011.1	52.20	2.38×2.26	ALESS061.1	50.80	2.43×2.27	ALESS098.1	55.80	2.48×2.28
ALESS013.1	50.10	2.38×2.25	ALESS063.1	50.50	2.43×2.27	ALESS099.1	54.50	2.48×2.27
ALESS014.1	50.20	2.39×2.26	ALESS065.1	52.20	2.43×2.27	ALESS102.1	54.30	2.48×2.27
ALESS015.1	51.30	2.39×2.26	ALESS066.1	49.70	2.43×2.27	ALESS103.3	53.90	2.49×2.27
ALESS017.1	50.10	2.39×2.26	ALESS067.1	51.00	2.43×2.27	ALESS107.1	57.90	2.50×2.27
ALESS018.1	49.80	2.39×2.26	ALESS068.1	52.60	2.42×2.27	ALESS110.1	56.20	2.51×2.28
ALESS019.1	52.20	2.39×2.26	ALESS069.1	53.10	2.43×2.27	ALESS112.1	53.30	2.51×2.28
ALESS022.1	51.20	2.40×2.26	ALESS070.1	52.80	2.43×2.27	ALESS114.1	58.30	2.51×2.28
ALESS023.1	52.10	2.40×2.26	ALESS071.1	52.60	2.43×2.27	ALESS115.1	54.70	2.50×2.28
ALESS025.1	51.60	2.40×2.26	ALESS072.1	52.00	2.43×2.27	ALESS116.1	54.90	2.52×2.28
ALESS029.1	51.10	2.40×2.26	ALESS073.1	53.30	2.43×2.27	ALESS118.1	56.80	2.52×2.28
ALESS031.1	53.90	2.40×2.26	ALESS074.1	51.30	2.44×2.27	ALESS119.1	54.60	2.51×2.28
ALESS035.1	52.90	2.41×2.26	ALESS075.1	52.90	2.45×2.26	ALESS122.1	57.30	2.52×2.28
ALESS037.1	50.20	2.40×2.26	ALESS076.1	51.80	2.44×2.27	ALESS124.1	55.70	2.53×2.28
ALESS039.1	51.80	2.41×2.26	ALESS079.1	51.20	2.45×2.27	ALESS126.1	56.10	2.53×2.28

2.3 IMAGING

Once all the data is corrected we proceed to create the images. We have two types of images. The first one is a collapsed image in right ascension and declination with no primary beam correction. The second one is a line cube where the third axis is the frequency corresponding to observations from ~ 137 GHz to ~ 153 GHz comprising four spectral windows. In both cases the task *CLEAN* from CASA was used. To create the collapsed images, inside the *CLEAN* task we set the mode to ‘*mfs*’. For all the spectral windows the cleaning process was carried out using a threshold of 6×10^{-4} mJy and a cell-size of 0.46 *arcsec*. The weighting was set to *Briggs* with *robust* 0.5 and *outer-taper* of [2.1 arcsec, 1.1 arcsec] for 500 iterations. Same parameter were used to create the line cubes, however in this case mode was set to ‘*frequency*’ because we want to map the intensity of the source at different frequencies. The *width* was set to 62.5 MHz corresponding to a binning of 54.5 kms^{-1} . All the parameters were taken from the original cleaning script provided by the ALMA observatory to properly achieve the same resolution and *rms* they report in the data sample. Though we can change these values and use different ones depending on our own goals, we think this settings are suitable for our propose given the quality of the data. All the images were inspected to check if the *RMS* was the same as the specified by ALMA in order to confirm that the calibration pipeline ran well. The values obtained were the same as shown in Table 1.

In Figure 7, we have an example of how two sources, **ALESS001.1** and **ALESS114.1** look like after the calibration process. The red dot shows the position in right ascension and declination of the pixel with maximum flux around the ALESS position reported by (Hodge et al, 2013). The white contours show the $-2, 3, 4, 5, 7, \dots \times rms$. The beam size is also shown in the left-bottom corner. We show these two sources because in some cases we don not detect any source with a high signal-to-noise ratio, then we need to double check. In this case, **ALESS001.1** is clearly detected while **ALESS114.1** is not. Therefore, we must select only those galaxies with a significant signal-to-noise ratio in order to analyze their spectrum to search for emission lines. The process to obtain the final sample and the imaging are described in the next section.

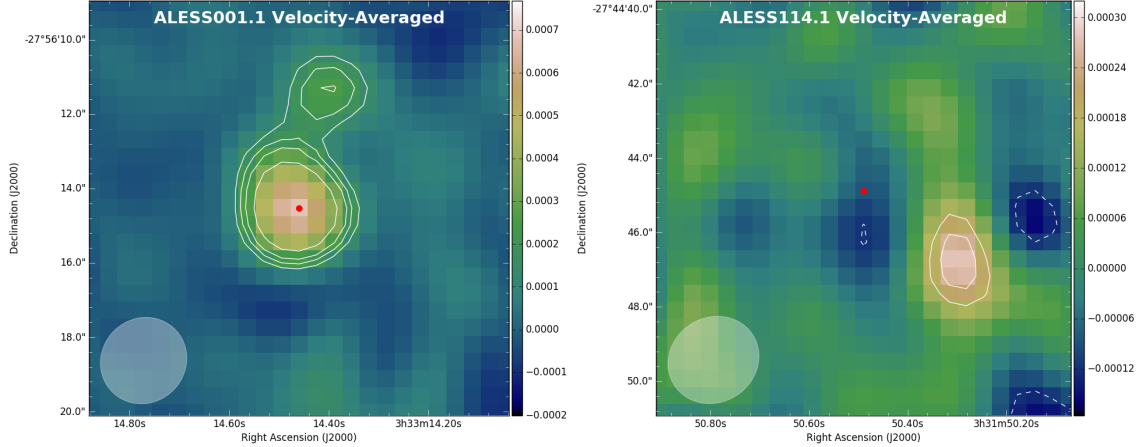


Figure 7: Velocity-Averaged maps of **ALESS001.1** and **ALESS114.1** in right ascension (*x*-axis) and declination (*y*-axis). The red dot marks the position of the pixel with maximum flux, while the white contours correspond to the $-2, 3, 4, 5, 7, \dots \times rms$. The white circle in the left-corner is the beam size as reported in Table 1. The color bar stands for the flux intensity in μJy

2.4 FINAL SAMPLE

As was seen before, not all the sources were clearly detected, only 51 out of 69. Then we need to select those sources which a *S/N* ratio above a given limit in order to guarantee images with low noise. Thus, those sources with $S/N > 4$ will be kept while those with $S/N < 4$ were left. Final sample obtained with this cut-off is consistent with the ALMA observatory data report provided with the observations, and it is composed of 51 sources. In Figure 8, Figure 9 and Figure 10, the final velocity-averaged maps are shown for this sub-sample, where the red dot indicates the pixel position with maximum flux obtained for $870\mu m$ observations in right ascension and declination of the source as reported by (Hodge et al, 2013), the white contours correspond to $-2, 3, 4, 5, 7, \dots \times rms$ and the white circle in the left-bottom side the beam size. In the next sections, all the study carried out on these sources is explained as the spectrum extraction, the fitting and physical properties of the objects.

In Table 2, we sum up the final sample and additionally the coordinates, photometric and spectroscopic redshift (if available) obtained from (Danielson et al, 2017), which we will use to analyze the different properties of these sub-sample ALESS sources.

Table 2: Final sample of ALESS sources with $S/N > 4$. The coordinates in right ascension and declination are shown taking from (Hodge et al. 2013) for $870\mu\text{m}$ observations. Additionally, the spectroscopic and photometric redshift from (Danielson et al. 2017) is also presented.

Name	RA (J2000)	DEC (J2000)	z_{phot}	z_{spec}	Name	RA (J2000)	DEC (J2000)	z_{phot}	z_{spec}
ALESS001.1	53.31027000	-27.93736600	4.340	4.9540	ALESS055.1	53.25924200	-27.67651300	2.050	1.3564
ALESS002.1	53.26118800	-27.94521100	1.960	2.1913	ALESS059.2	53.26589700	-27.73839000	2.090	
ALESS003.1	53.33960300	-27.92230400	3.900	4.2373	ALESS061.1	53.19112800	-28.00649000	6.520	4.4190
ALESS005.1	52.87046700	-27.98584000	2.860		ALESS063.1	53.28519300	-28.01217900	1.865	
ALESS006.1	53.23733100	-28.01685600	0.450	2.3338	ALESS067.1	53.17998100	-27.92064900	2.135	2.1230
ALESS007.1	53.31424200	-27.75675000	2.495	2.6923	ALESS068.1	53.13888800	-27.65377000	-3.600	
ALESS009.1	53.04724400	-27.86998100	4.500		ALESS069.1	52.89073100	-27.99234500	2.340	4.2082
ALESS010.1	53.07941800	-27.87078100	2.020	0.7616	ALESS070.1	52.93342500	-27.64320000	2.275	2.0918
ALESS011.1	53.05768800	-27.93340300	2.825	2.6832	ALESS072.1	53.16832200	-27.63280700	-4.150	
ALESS013.1	53.20413200	-27.71438900	3.250		ALESS073.1	53.12204600	-27.93880700	5.180	4.7640
ALESS014.1	52.96871600	-28.05530000	4.465		ALESS076.1	53.38473100	-27.99878600	-4.500	3.3895
ALESS015.1	53.38903400	-27.99154700	1.925		ALESS079.1	53.08806400	-27.94083000	2.045	
ALESS017.1	53.03041000	-27.85576500	1.505	1.5397	ALESS080.1	52.92834700	-27.81024400	1.960	4.6649
ALESS018.1	53.02034300	-27.77992700	2.045	2.2520	ALESS084.1	52.97709000	-27.85156800	1.915	3.9651
ALESS019.1	53.03440100	-27.97060900	2.410		ALESS088.1	52.97817500	-27.89485800	1.835	1.2679
ALESS022.1	52.94549400	-27.54425000	1.875		ALESS098.1	52.87465400	-27.95631700	1.630	1.3735
ALESS023.1	53.05003900	-28.08512800	4.990		ALESS107.1	52.87708200	-27.86364700	3.745	2.9965
ALESS025.1	52.98699700	-27.99425900	2.235	2.8719	ALESS110.1	52.84441100	-27.90478400	2.545	
ALESS029.1	53.40374900	-27.96925900	2.655	1.4389	ALESS112.1	53.20359600	-27.52036200	1.950	2.3154
ALESS031.1	52.95744800	-27.96132200	2.885		ALESS114.1	52.96036000	-27.74592900	-3.000	
ALESS035.1	52.79377600	-27.62094900	-3.300		ALESS115.1	53.45707000	-27.70960900	-3.450	3.3631
ALESS037.1	53.40059800	-27.89738300	3.530		ALESS116.1	52.97634200	-27.75803900	3.540	
ALESS039.1	52.93762900	-27.57687100	2.440		ALESS118.1	52.84134700	-27.82816100	2.260	2.3984
ALESS045.1	53.10525500	-27.87514800	2.340		ALESS119.1	53.23599300	-28.05698800	3.500	
ALESS049.1	52.85299800	-27.84640600	2.760	2.9417	ALESS122.1	52.91476800	-27.68879200	2.060	2.0252
ALESS051.1	52.93775400	-27.74092200	1.220	1.3638	ALESS124.1	53.01684300	-27.60176900	6.065	

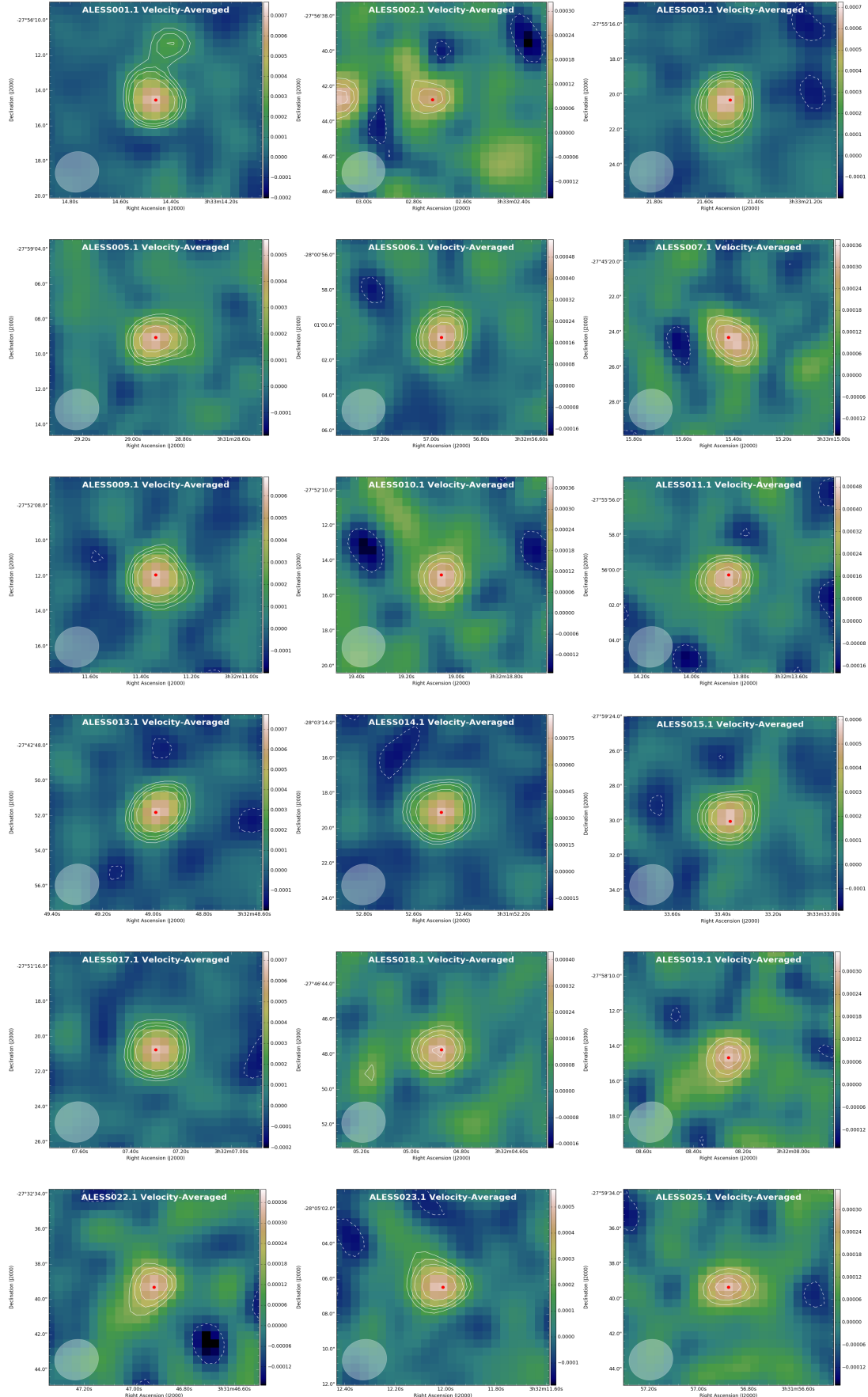


Figure 8: Velocity-Averaged maps for ALESS001.1 to ALESS025.1 in right ascension (x -axis) and declination (y -axis). The red dot marks the position of the pixel where flux is maximum, while the white contours correspond to $-2, 3, 4, 5, 6, 7 \dots \times rms$. The white circle in the left-corner is the beam size as reported in Table 1. The color bar stands for the flux intensity in μJy .

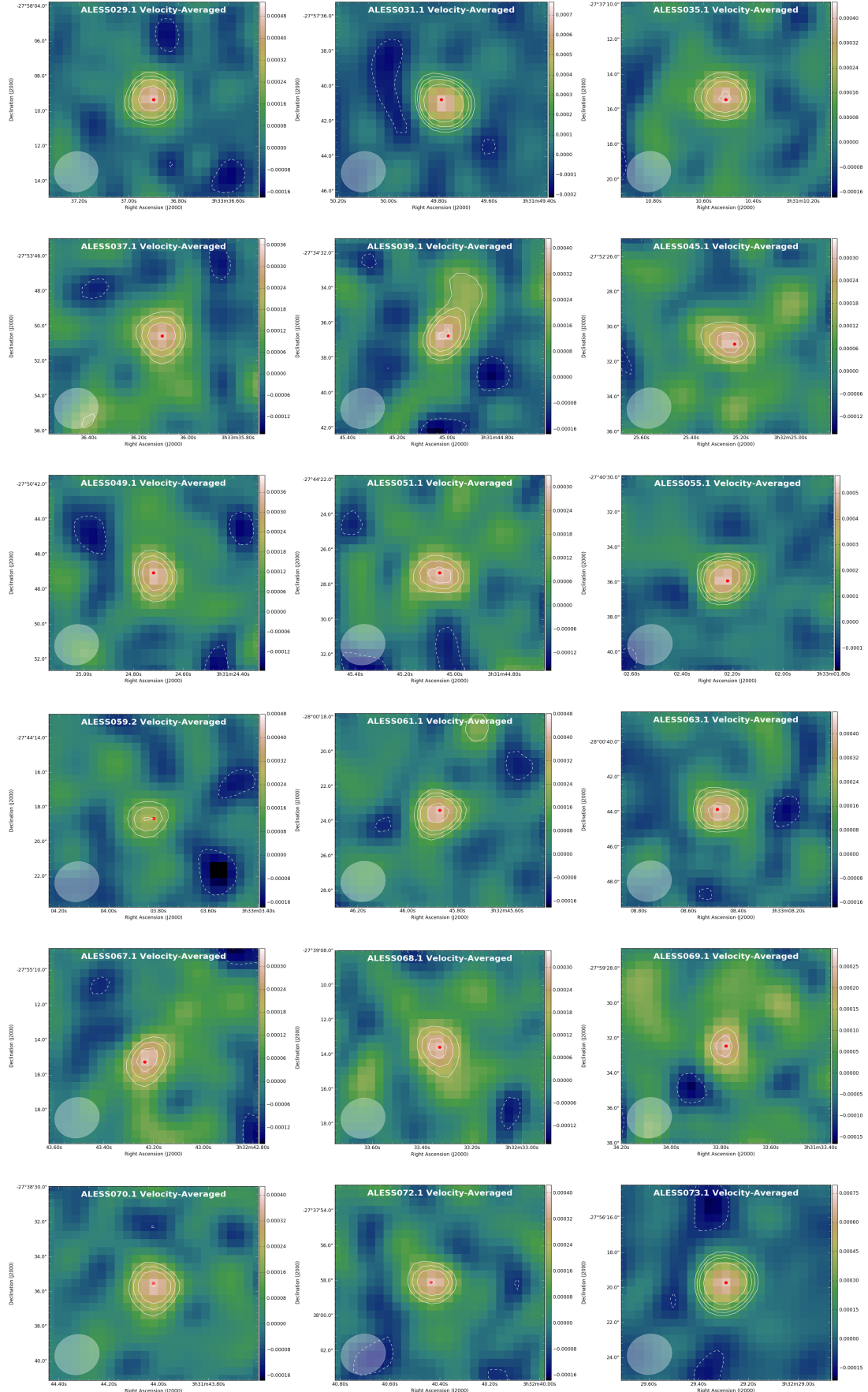


Figure 9: Velocity-Averaged maps for ALESS029.1 to ALESS073.1 in right ascension (x-axis) and declination (y-axis). The red dot marks the position of the pixel where flux is maximum, while the white contours correspond to $-2, 3, 4, 5, 7 \dots \times rms$. The white circle in the left-corner is the beam size as reported in Table 1. The color bar stands for the flux intensity in μJy

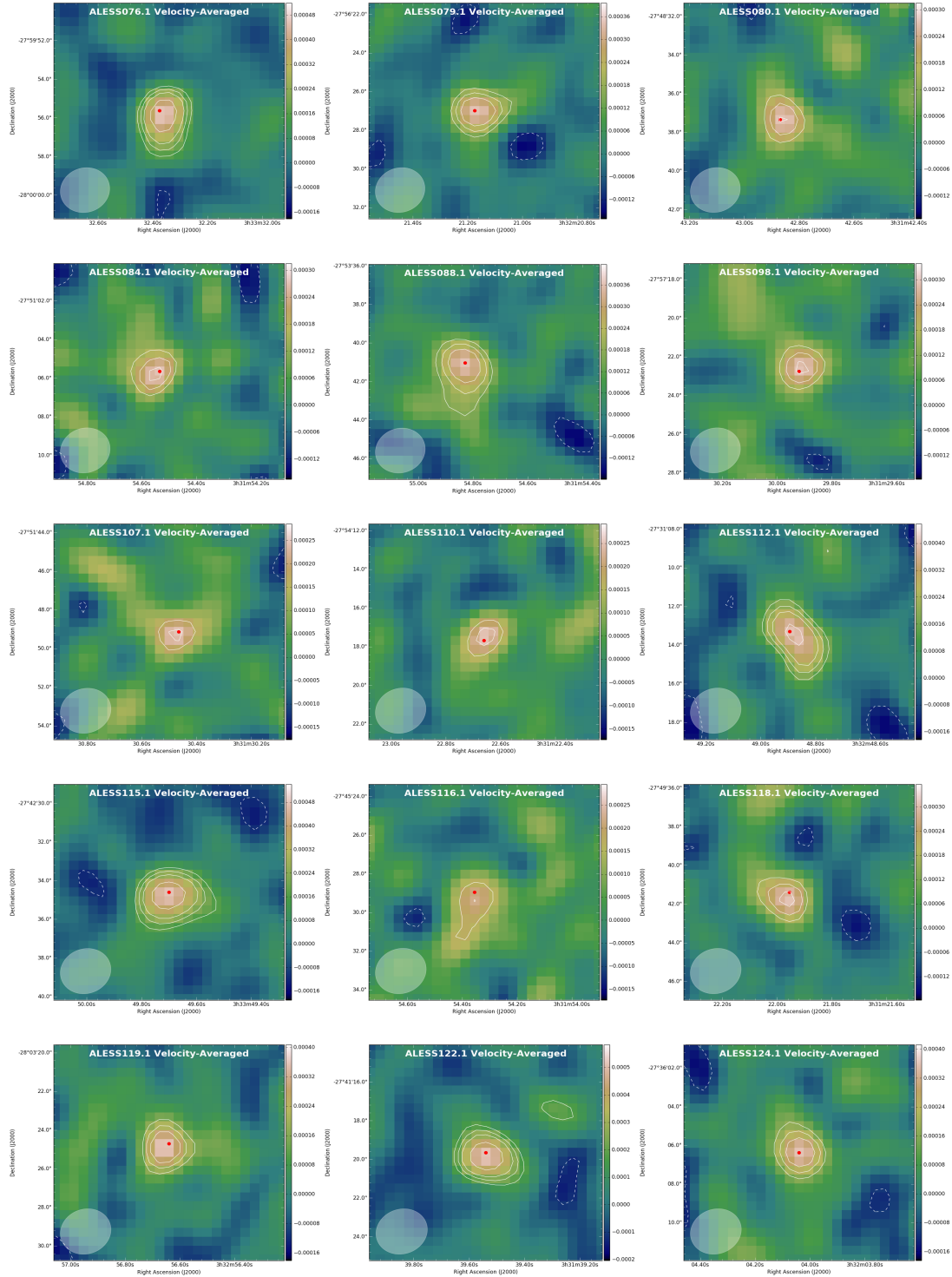


Figure 10: Velocity-Averaged maps for ALESS076.1 to ALESS124.1 in right ascension (x -axis) and declination (y -axis). The red dot marks the position of the pixel where flux is maximum, while the white contours correspond to $-2, 3, 4, 5, 7\dots \times rms$. The white circle in the left-corner is the beam size as reported in Table 1. The color bar stands for the flux intensity in μJy

SPECTRAL LINE ANALYSIS

3.1 INTRODUCTION

In this chapter, the method used to obtain the spectra for the final sample of ALESS sources is addressed. A robust description of how the spectra was extracted and the lines were fitted is presented to clarify the different procedures carried out to characterize the sources. In order to guarantee reliable line detections we decided to compare the continuum-fit with line-fit using the χ^2 -difference assuming that a line is real if $\Delta\chi^2$ is larger than 25 which translates into a 5σ detection. Only two sources out of the 51 selected in [Chapter 2](#) satisfied our conditions. New insights about the spectroscopic redshift of ALESS070.1 are discuss. These sources were checked to have a counterpart in the Spitzer/IRAC survey to guarantee real detections, thus continuum and line maps are also presented.

3.2 SPECTRUM EXTRACTION

As was shown in [Chapter 2](#), the final sample of ALESS sources after applying a cut-off in the signal-to-noise ratio is conformed by 51 targets (see [Table 2](#)). In order to extract the spectrum for each source, a circular region was selected centred at the coordinates in RA and DEC of the sources as reported in ([Hodge et al, 2013](#)) for $870\mu\text{m}$ observations as a first guess for the possible, real pixel position of the maximum flux in our observation. Then, the spectrum was selected as a point spectrum from the pixel with maximum flux after performing a statistical analysis of the flux pixel by pixel inside the circular region using CASA. Two different methods were addressed varying the size of the circle because there could be small off-sets between the maximum emission of the galaxy at our frequency and the centre coordinates of the source. First we decided to use a circular radius of 1.0 arcsec, and searched for the pixel value corresponding to maximum emission inside that circle. Once the pixel value is obtained, we subtract all the different values of the flux (Stokes I) along the line cube image (i.e. along the frequency axis). The same procedure was carried out with a circular region of radius 0.5 arcsec in order to confirm whether reducing the aperture would change or not the pixel value for maximum flux due to some coordinates off-set. However, both methods were consistent and even using larger radius values gave the same pixel value. Afterwards we checked the sources to be resolved or not, deconvolving the beam and trying to fit the major and minor axis for our galaxies. However, the image component deconvolved from the beam resulted in a point source which had almost the same size or smaller than the beam size . As our sources are not resolved, so we decided to use the peak spectrum as described above instead of the integrated spectrum because in our case is more representative.

In [Figure 11](#), we have ALESS031.1 and ALESS039.1 as an example of the procedure described above. The black continuous lie corresponds to the 0.5 arcsec circle while the dashed line to the 1.0 arcsec. The red point marks the position of the pixel where the maximum flux was coming from. This sources were chosen as example because ALESS31.1 is the type of source in our data

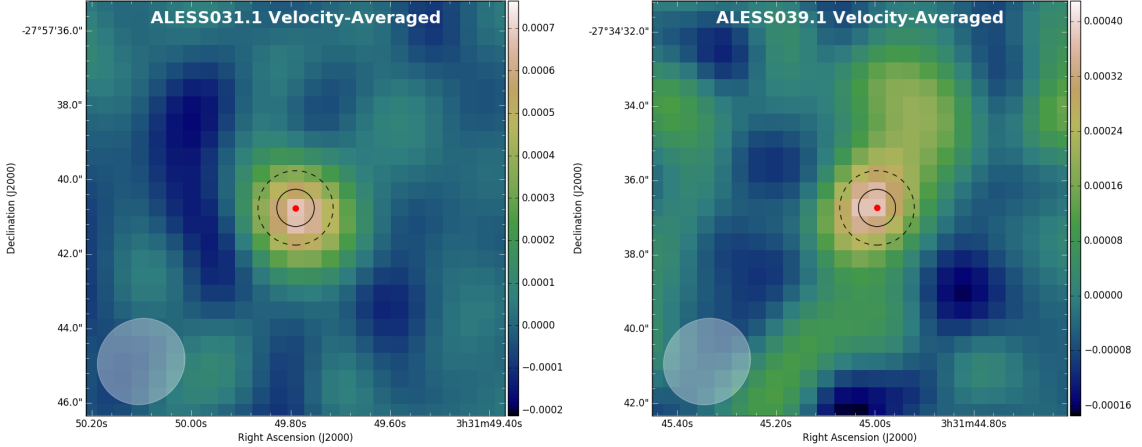


Figure 11: Circular regions used to constrained the region around the position of each source to look for the maximum flux. *left* ALESS031.1 and *right* ALESS039.1. In the case of ALESS039.1 there is a close companion which can interfere with the pixel value for the maximum flux, so both circles are large enough to contain the information of the right source and avoid possible contamination from nearby sources. the black solid circle corresponds to a radius of 0.5 arcsec while the dashed circle to a radius of 1.0 arcsec. The red dot marks the position of the maximum emission pixel in our observations. The beam size is shown in the left corner.

which is well-defined with no other prominent sources around while ALESS39.1 has a close companion which makes the source a little bit extended. The size of the circular regions were chosen to contain all the information of one source in order to avoid mixing information from any other source nearby which could be somewhat brighter and then causing the pixel value to be chosen incorrectly. Once the pixel value was chosen, the flux (mJy/beam) at a given frequency (GHz) was extracted and stored in a file. This files were analyzed after to search for any emission line that could have been detected during the survey. The fitting process and method used to accept or reject a given line are thoroughly explained in the next section.

3.3 LINE FITTING

Once the flux values at each frequency are extracted we need to find a way to fit the possible emission lines present. Each spectrum was divided into two ranges, one from 137 GHz to 141 GHz which includes the spectral windows ‘0’ and ‘1’, and other one from 149 GHz to 153 GHz including spectral windows ‘2’ and ‘3’. Although all the results were carried out separately for both ranges, the same procedure was performed using the complete frequency range to check possible differences in the result. However, because the frequencies between spectral window ‘1’ and ‘2’ has no information because the observations were performed in this way, but both methods led the same results. Later, A subset of possible molecule transitions were chosen from ([Spilker et al, 2014](#)) and are summarized in [Table 3](#). We decided to use these transitions because they are the result of stacking several sources in order to obtain the line intensity of a given molecule present in a SMG. Thus, we expect any line present in our observations to be at least consistent with the values reported by ([Spilker et al, 2014](#)). The expected frequency (i.e. observed frequency) was obtained using [Equation 3.1](#), where the redshift corresponds to the spectroscopic redshift listed in [Table 2](#) or the photometric in case the spectroscopic is unknown.

Table 3: Transitions with fine or hyperfine structure taken from (Spilker et al, 2014). Frequencies correspond to the rest frame frequency in GHz.

Line	ν_{res} (GHz)	Line	ν_{res} (GHz)	Line	ν_{res} (GHz)	Line	ν_{res} (GHz)	Line	ν_{res} (GHz)	Line	ν_{res} (GHz)
CO(1 – 0)	115.2712	HCN(5 – 4)	443.1161	H ₂ O(4 _{1,4} – 3 _{2,1})	380.1974	OH(446)	446.2910	CS(7 – 6)	342.8830	CCH(5 – 4)	436.6604
CO(2 – 1)	230.5380	HCN(6 – 5)	531.7164	H ₂ O(4 _{2,3} – 3 _{3,0})	448.0011	CN(N = 3 – 2)	340.2478	CS(8 – 7)	391.8470	CCH(6 – 5)	523.9704
CO(3 – 2)	345.7960	HCN(7 – 6)	620.3040	H ₂ O(5 _{3,3} – 4 _{4,0})	474.6891	CN(N = 4 – 3)	453.6067	CS(10 – 9)	489.7510	CCH(7 – 6)	611.2650
CO(4 – 3)	461.0408	HCN(8 – 7)	708.8770	H ₂ O(1 _{1,0} – 1 _{0,1})	556.9360	CN(N = 5 – 4)	566.9470	CS(11 – 10)	538.6888	CCH(8 – 7)	698.5416
CO(5 – 4)	576.2679	HNC(3 – 2)	271.9811	H ₂ O(2 _{1,1} – 2 _{0,2})	752.0331	CN(N = 6 – 5)	680.2641	CS(12 – 11)	587.6162	H21 α	662.4042
CO(6 – 5)	691.4731	HNC(4 – 3)	362.6303	H ₂ O ⁺ 604	604.6786	SIO(7 – 6)	303.9270	CS(13 – 12)	636.5318	H22 α	577.8964
¹³ CO(3 – 2)	330.5880	HNC(5 – 4)	453.2699	H ₂ O ⁺ 607	607.2273	SIO(8 – 7)	347.3306	CS(14 – 13)	685.4348	H23 α	507.1755
¹³ CO(4 – 3)	440.7652	HNC(6 – 5)	543.8976	H ₂ O ⁺ 631	631.7241	SIO(9 – 8)	390.7284	CS(15 – 14)	734.3240	H24 α	447.5403
¹³ CO(5 – 4)	550.9263	HNC(7 – 6)	634.5108	H ₂ O ⁺ 634	634.2729	SIO(10 – 9)	434.1196	NH ₃ (1 ₀ – 0 ₀)	572.4982	H25 α	396.9008
¹³ CO(6 – 5)	661.0673	HNC(8 – 7)	725.1073	H ₂ O ⁺ 721	721.9274	SIO(11 – 10)	477.5031	N ₂ H ⁺ (3 – 2)	279.5117	H26 α	353.6227
C ¹⁸ O(3 – 2)	329.3305	HCO ⁺ (3 – 2)	267.5576	H ₂ O ⁺ 742	742.1090	SIO(12 – 11)	520.8782	N ₂ H ⁺ (4 – 3)	372.6725	H27 α	316.4154
C ¹⁸ O(4 – 3)	439.0888	HCO ⁺ (4 – 3)	356.7342	H ₂ O ⁺ 746	746.5417	SIO(13 – 12)	564.2440	N ₂ H ⁺ (5 – 4)	465.8250	H28 α	284.2506
C ¹⁸ O(5 – 4)	548.8310	HCO ⁺ (5 – 4)	445.9029	H ₂ O ⁺ 761	761.8188	SIO(14 – 13)	607.5994	N ₂ H ⁺ (6 – 5)	558.9667		
C ¹⁸ O(6 – 5)	658.5533	HCO ⁺ (6 – 5)	535.0616	LiH(1 – 0)	443.9529	SIO(15 – 14)	650.9436	N ₂ H ⁺ (7 – 6)	652.0959		
CI(1 – 0)	492.1606	HCO ⁺ (7 – 6)	624.2085	CH(532)	532.7239	SIO(16 – 15)	694.2754	N ₂ H ⁺ (8 – 7)	745.2103		
HCN(3 – 2)	265.8864	HCO ⁺ (8 – 7)	713.3414	CH(536)	536.7614	SIO(17 – 16)	737.5939	CCH(3 – 2)	262.0042		
HCN(4 – 3)	354.5055	H ₂ O(5 _{1,5} – 4 _{2,2})	325.1529	OH(425)	425.0363	CS(6 – 5)	293.9122	CCH(4 – 3)	349.3387		

$$1 + z = \frac{\nu_{\text{emi}}}{\nu_{\text{obs}}} \quad (3.1)$$

In Figure 12 we have ALESS006.1 and ALESS059.2 with the position of expected molecule transitions from (Spilker et al, 2014) plotted on the given frequency range. The vertical lines correspond to the transitions and the continuous green line to the source spectrum. The vertical axis is the flux in mJy/beam while the horizontal axis corresponds to the frequency in GHz. Once the expected frequency position is known i.e the ν_{obs} in Equation 3.1, we can use it as a initial guess in order to fit any feature around it. However, the fitting-script fits the most reliable feature close to the line, then even if the redshifts (i.e spectroscopic or photometric) are wrong, the most conspicuous feature in the spectrum is fitted. Thus, if some discrepancy pops up between the expected line and a given prominent feature in the spectrum we can start thinking about how well the redshift is measured for a given source as provided by (Danielson et al, 2017) and probably better constrain it through our spectroscopic analysis.

We used two fitting functions: a *Gaussian* for the emission line and a *Line* to trace the continuum. In Equation 3.2 the Gaussian amplitude ‘A’ was constrained to be positive, the mean frequency ‘ μ ’ was set to the expected frequency and the constant ‘C’ also to be positive’. In the case of linear-fit (Equation 3.3) we used just a constant, since over the 7.5 GHz band width the change in slope is negligible (specially given the noise).

$$\mathbf{G}(A, \mu, \sigma, C; x) = Ae^{-\frac{x-\mu}{2\sigma^2}} + C \quad (3.2)$$

$$\mathbf{L}(B) = B \quad (3.3)$$

To accept or reject an emission line we will compare how reliable is the Gaussian fit over the continuum fit. This was addressed using the χ^2 -difference which is directly related to the signal-to-noise ratio of our detections and the relative error. We described it in detail in the next subsection.

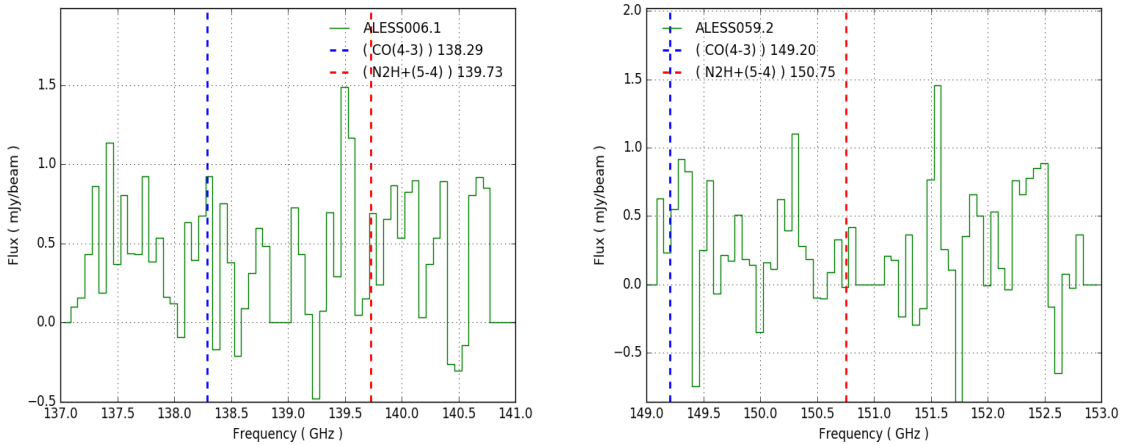


Figure 12: Likely molecules to be present in the ALESS sources plotted along the source spectrum. The red and blue vertical lines represent the most likely emission lines to be present given the redshift of the source. The green continuous line is part of the spectrum only comprising the spectral range where a line was predicted to be in. *left* ALESS006.1 in a frequency range containing spectral windows ‘0’ and ‘1’. *right* ALESS059.2 in a frequency range containing spectral windows ‘2’ and ‘3’.

3.3.1 χ^2 difference and goodness of fit

One of the main goals of this project is to properly analyze and treat the spectra obtained. As was shown in [Section 3.3](#) and later explained in [Sub-section 3.3.2](#), we will fit a Gaussian to the possible spectral lines in our spectra. Then, we need to test how well is this fit for a given feature in order to decide if a line is real or not compared to the rest of the data. This process will be performed using the well known χ^2 -squared test of goodness of fit, due to the fact that it directly relates to the signal-to-noise of our detections.

The χ^2 -squared test is used when we have a nominal variable and we want to see whether the observations in each category fits a theoretical expectation and the sample size is large. This test as most of the statistical tests, does not calculate directly the probability of obtaining the observed results. Instead, it uses the data we have measured to compute a test statistic that measures how far the observed are from the null expectation. Then, it uses a mathematical relation, which in this case is the ‘ χ^2 -squared’ distribution to estimate the probability of obtaining the value of the test statistic. The test statistics, on the other hand, is obtained taking our observations and subtracting from them the expected number. In both cases, the expectation and observed values could be a number or just a function. Then we square the difference and weight by the expected number. Finally, we add up all this values to compute the final value as can be seen in [Equation 3.4](#).

$$\chi^2 = \sum \frac{(\text{Observed} - \text{Expected})^2}{\text{Expected}} \quad (3.4)$$

The larger the deviation from the null hypothesis (assuming that there is or not a significant difference between the expected and observed values), the larger the difference between the observed and expected values. According to this reasoning the value we expect for the χ^2 must be as small as possible in order guarantee that our expectations are pretty close to our observations.

Thus, what we look for is to minimize [Equation 3.4](#).

From other point of view, this can be seen as the sum of the squared deviations of points from a given function, normalized by the variances. Then we have a direct relation between the χ^2 and the relative error which is defined as ratio of the standard deviation to the mean. More importantly, this directly translates into a relation to the signal-to-noise which is basically the inverse of the relative error. Hence, minimizing the χ^2 can be understood as reducing the relative error and increasing the signal-to-noise ratio.

As will be explain in [Sub-section 3.3.2](#), we want to compare two fits. Therefore, we want to find the minimum value between both χ^2 , making the $\Delta\chi^2$ as large as possible to guarantee enough signal-to-noise in our observations. We decided to apply this method in our data, in some way following ([Swinbank et al, 2012](#)), because the continuum in their data is not so strong as is our case. Then, we decided to fit a line to the continuum without any slope and a Gaussian to the line, to find any emission lines in the ALESS sources sub-sample we have. In [Figure 13](#), we show the fitting performed by ([Swinbank et al, 2012](#)) in order to clarify what we expect in our observations and how we expect the fits to look in the end.

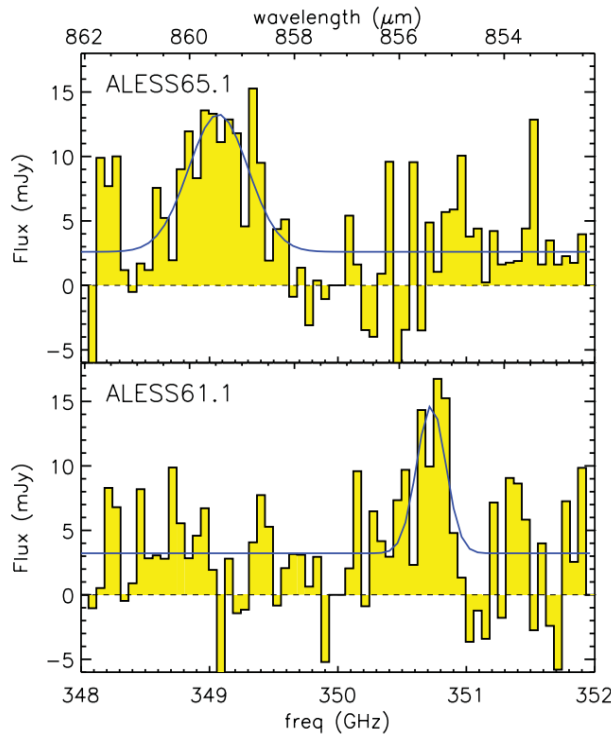


Figure 13: *Top:* ALESS65.1 spectrum with Gaussian fitting. *Bottom:* ALESS61.1 spectrum with Gaussian fitting. In both cases the y-axis is expressed in mJy and the x-axis in GHz. Both detections satisfy a criterion of having a $\Delta\chi^2 > 20$ which corresponds to $\sigma > 4$ detection as shown in ([Swinbank et al, 2012](#)).

This method will be follow to analyze our data, where we also take as real detections only those sources where the $\Delta\chi^2 > 25$ to guarantee detections above $\sigma = 5$ and a good signal-to-noise ratio. This process is explained immediately.

3.3.2 Acceptance method and Fitting parameters

As has been shown in Sub-section 3.3.1, we need to minimize the χ^2 to properly say that a certain fitting function is representative of the present feature or not. However, we have two functions so we need to compare them and see which one is the best. According to this if the χ^2 -difference between the line and Gaussian fitting is positive, we say the Gaussian fit is better than the line fit because the Gaussian χ^2 is smaller than the line χ^2 , thus the line could be partially accepted. If the χ^2 -difference between the line and Gaussian fitting is negative, then the line fitting is better so the emission line is not reliable. We must guarantee good signal-to-noise ratio, so the χ^2 difference must be larger than 25 to be accepted which corresponds to a 5σ detection. This is summed up in Equation 3.5. *In concreto*, if the χ^2 difference is positive and larger than 25 the line is assumed to be a real detection. We applied this method to our 51 targets using the possible emission lines expected in each case given the redshift of the source. The parameters retrieved in each case are the Gaussian amplitude ‘A’, the mean frequency μ , the constant C , the variance σ , and the constant ‘B’. Using this, we are able to compute the full-width half maximum **FWHM** of the line given by Equation 3.7, where σ is given in $km\ s^{-1}$. To change from frequency to velocity we used the well-known radio velocity definition (see Equation 3.7) which will facilitate calculations of different physical properties for the sources.

$$\begin{aligned} \chi_{\text{line}}^2 - \chi_{\text{gaussian}}^2 &> 0 & ; & \text{ Accepted} \\ \chi_{\text{line}}^2 - \chi_{\text{gaussian}}^2 &< 0 & ; & \text{ Rejected} \end{aligned} \quad (3.5)$$

$$FWHM \approx 2.35\sigma \quad (3.6)$$

$$v_{\text{rad}} = c \left(1 - \frac{\nu}{\nu_o} \right) \quad (3.7)$$

Most of the galaxies which had a possible emission line did not satisfy the criteria (i.e. χ^2 differences was either less than 20 or negative) so they were rejected. In most of the cases it was below 10. However, two sources ALESS070.1 and ALESS122.1 did show an evident line and satisfied the criteria imposed above. Then, we only ended up with the two reliable detections in two sources of the 51 targets clearly detected in this survey. In Figure 14 we have the final spectrum for the last two sources where the *x-axis* corresponds to the frequency in GHz and the *y-axis* to the flux in mJy/beam. The green line represents the Gaussian fit and the dashed-yellow line the continuum fit shown above in Equation 3.2 and Equation 3.3. The black vertical line is the most likely transition expected from Table 3 for both galaxies which led to the green fit after using this frequency as initial guess. We see that for ALESS122.1 the fit matches really well for a CO(4 – 3) transition whilst not so well for ALESS070.1, though is really prominent.

As was briefly introduced in Chapter 1, (Danielson et al, 2017) carried out an optical spectroscopic study of the ALESS-sources in order to obtain well-determined spectroscopic redshift as part of the zLESS project. The details of their observations are shown right away. The observing campaign was addressed using the FOcal Reducer and low dispersion Spectrograph (FORS2) and Visible MultiObject Spectrograph (VIMOS) on VLT. However, in order to increase the wavelength coverage and to supplement the observations also the XSHOOTER on VLT, the

Gemini Near-infrared Spectrograph (GNIRS) and the Multi-Object Spectrometer for Infra-Red Exploration (MOSFIRE) were used. They observed around 100 hours each with VIMOS and FORS because SMGs typical redshifts are expected to have Ly α , UV ISM lines and [OIII] emission which could be really faint. Using FORS2, they observed on every source for 4.5 hours in wavelengths $\lambda = 3300 - 11000\text{\AA}$ and a typical resolution of $R \sim 660$. Using VIMOS they used the OS-blue order sorting filter ($\sim 4000 - 6700\text{\AA}$) with a resolution of $R \sim 180$ and exposure time of 3 – 9 hours. As was mentioned above, to complement these observations they used the XSHOOTER to target 20 ALESS SMGs with 4×600 s exposures per source, covering wavelength ranges of $3000 - 5600\text{\AA}$, $5500 - 10200\text{\AA}$ and $10200 - 24800\text{\AA}$ for the UV (UVB), visible (VIS) and near-infrared (NIR) arms respectively. With the MOSFIRE spectrograph on Keck I they targeted 36 SMGs in bands H($1.46 - 1.81\mu\text{m}$) and K($1.93 - 2.45\mu\text{m}$) with resolution $R \sim 3270$. The exposure time was set to 120s in H-band and 180s in K-band per source. DEIMOS on Keck II and GNIRS to target 71 and eight SMGs respectively. With DEIMOS they used 1200s exposure time on source with a resolution of $R \sim 3000$ and with GNIRS ~ 1.5 hour per source with $R \sim 1700$ resolution. Only two SMGs redshifts were obtained with ALMA [CII] observations (ALESS61.1 and ALESS65.1).

Aside from this, we must have in mind that all the spectroscopic redshifts shown in [Table 2](#) have a quality factor denoted by Q (see [Danielson et al, 2017](#)) which goes from 1 to 4, where Q = 1 is a really well measured and trusty spectroscopic redshift, Q = 2 corresponds to a redshift measured from only one or two strong lines, Q = 3 is a tentative redshift measured based on one or two very faint features and Q = 4 for sources which no redshift could be determined. For our two sources, we must say that in the case of ALESS070.1 Q = 3, meaning that the possible line used is too faint, so in that case the redshift used to predict the position of the line (black vertical line in [Figure 14](#)) was the photometric redshift. In the case of ALESS122.1, Q = 1 then in this case we trust completely in the spectroscopic redshift. The spectra provided by ([Danielson et al, 2017](#)) are shown in [Figure 15](#) for ALESS070.1 and ALESS122.1. In [Sub-section 3.3.3](#) the process carried out to study this discrepancy is addressed in more detail. Measuring redshifts for SMGs is a really hard task. This demands a lot of telescope time and sometimes these galaxies do not have an evident optical counterpart to compare with. Performing serendipitous blind line search with ALMA is a good method to overcome this issue because we do not need to target a special emission line but we can observe different emission lines in a given band width which helps us to find the spectroscopic redshifts with high accuracy.

In [Table 4](#), we summarize the fitting parameters for our two line detections. These values will be used throughout the next sections to compute different physical properties of these two SMGs.

After finding a possible discrepancy due to the lack of information in the redshift for ALESS070.1 we decided to double check the spectra available for these sources. In [Figure 15](#) the 1-D and 2-D spectra are shown for both sources. In both cases, we present the flux versus frequency for 1-D spectrum and pixel value versus frequency in the case of the 2-D spectrum. For ALESS070.1, the possible transition line corresponds to Lyman α , however the spectrum it is too noisy and we cannot conclude anything neither from the 1-D nor the 2-D spectrum. If we do not use the redshift found by ([Danielson et al, 2017](#)) but the one we find using the mean frequency of the line from our fitting, we get the line position shifted ([Figure 15 left-side](#)) but once again no special feature which could tempt us to say that the quality factor for this source could improve. Then, for ALESS070.1 we decided to use both the photometric redshift and our measured redshift for later comparisons. For ALESS122.1, we clearly see different emission and absorption lines (CII,

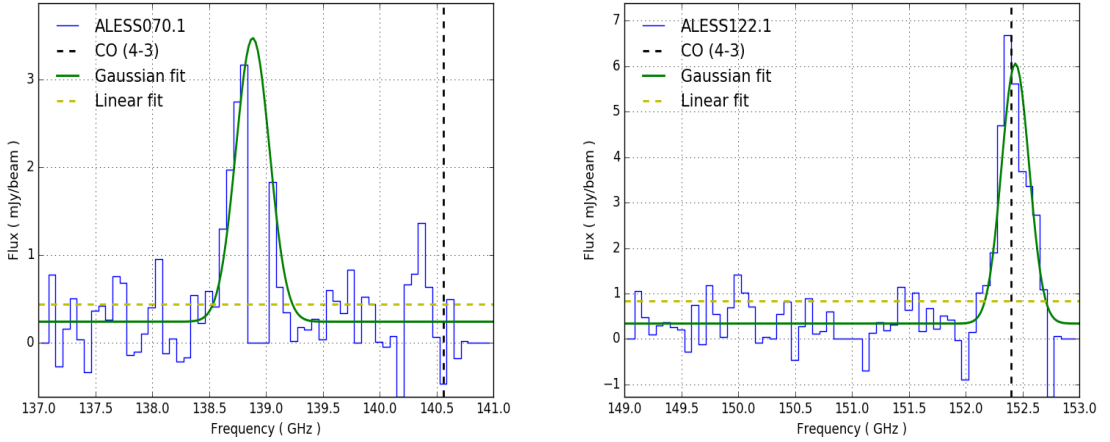


Figure 14: ALESS070.1 and ALESS122.1 spectrum. In the *x*-axis the frequency in GHz while in the *y*-axis the flux in mJy/beam. The green line represents the Gaussian fit while the dashed-yellow line the continuum. The vertical black line corresponds to the most likely molecule transition expected given the spectroscopic redshift for ALESS122.1 and the photometric redshift for ALESS070.1. In both cases CO(4 – 3) is the possible molecular transition.

Table 4: Fitting parameters obtained for ALESS070.1 and ALESS122.1. The redshift z corresponds to the photometric for ALESS070.1 and the spectroscopic for ALESS122.1 as reported by (Danielson et al, 2017) while the z (mean frequency) corresponds to our measurements through the CO detection.

Name	ALESS070.1	ALESS122.1
Amplitude A (mJy/beam)	3.24 ± 0.40	5.72 ± 0.39
Mean frequency μ (GHz)	138.88 ± 0.02	152.44 ± 0.01
Variance σ	0.15 ± 0.01	0.12 ± 0.01
Constant C (mJy/beam)	0.23 ± 0.06	0.34 ± 0.09
Constant B (mJy/beam)	0.44 ± 0.09	0.83 ± 0.19
FWHM (GHz)	0.35 ± 0.03	0.29 ± 0.02
FWHM (km s^{-1})	758 ± 74	621 ± 41
$\Delta\chi^2$	~ 31	~ 101
z	2.28	2.0232
z (mean frequency)	2.3197	2.0252

CIII, CIV, SiII, SiIV and HeII) and a strong blue continuum which gives rise to different values of redshift but pretty close to each other and in average equal to the redshift reported by this author. Then, we will keep on working with this spectroscopic redshift. In both cases we drew the lines for the possible line positions as shown in right-side plots. Additionally, we plotted in the left-side the line position using the redshift we found through the fitting in Table 4. Although for ALESS122.1 the change is not noticeable, for ALESS070.1 as mentioned before there is a shift which yields to no better conclusions about its redshift.

Summing up, all the values presented in Table 4 will be used to compute the most relevant physical properties in order to characterize this two sources, because at least for ALESS122.1 the results are in agreement with values reported in the literature and for ALESS070.1 our results probably show new insights about the distance of this source adding valuable information. In Sub-section 3.3.3 we address the process we performed to double check ALESS070.1.

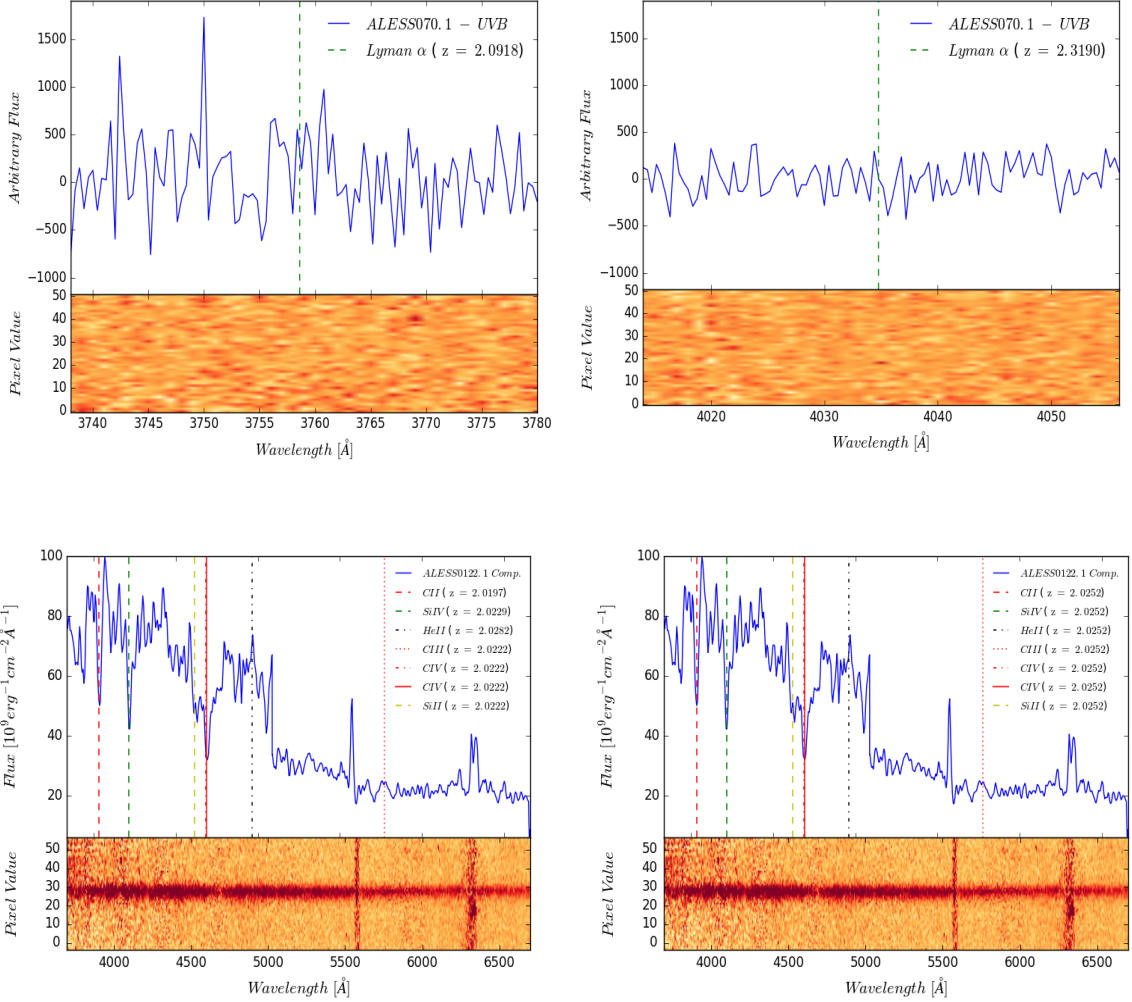


Figure 15: ALESS070.1 and ALESS122.1 spectra in the optical. *top*: ALESS070.1 1-D (flux vs frequency) and 2-D (pixel value vs frequency) spectrum obtained with VLT/FORS2 and VLT/XSHOOTER. *bottom*: ALESS122.1 1-D (flux vs frequency) and 2-D (pixel value vs frequency) spectrum obtained with VLT/FORS2 and VLT/VIMOS. Vertical lines correspond to most likely transitions as presented by (Danielson et al, 2017). Difference between *left* and *right* images is the line position which was computed using different values of redshift. In the *left* we show the original values obtained by (Danielson et al, 2017) while in the *right* we used the redshift found using the mean frequency obtained from the fitting as reported in Table 4.

3.3.3 Spectroscopic redshift for ALESS070.1

As has been presented above, for ALESS070.1 we cannot conclude that the spectroscopic redshift reported by (Danielson et al, 2017) is reliable. However, even using the photometric one the most likely transition expected from (Spilker et al, 2014) lies close to the spectral window gap (see Figure 16) in a place where no conspicuous emission is visible but close to the really prominent feature. The position of each spectral window is decided by the P.I. of the project. As these observations were not targeted to observed a given spectral line but dust continuum, if any line is present there is a chance that it falls exactly in between the spectral window gaps. This is basically the case of ALESS070.1. In spite of this, due to the conspicuous emission line present in Figure 14 we derived a redshift using a Gaussian-fit and taking the mean frequency as the observed frequency in Equation 3.1. The redshift found was computed using the CO(4-3) transition and its

value is closer to the photometric redshift reported by (Danielson et al, 2017) and at least between the upper limit error. To tackle down this problem and to be pretty sure that our observation corresponds to a CO(4-3) transition, we studied the bunch of possible emission lines which could lie near this emission feature using the photometric and spectroscopic redshift. In the end, comparing the chance to detect the possible obtained emission lines to CO transitions were less likely to be detected because in any case the CO line was pretty close, so if we observe any other molecule emission, the CO line should be present because they are expected to be brighter in comparison to any other emission lines as shown in (Spilker et al, 2014). Even if a given line were supposed to be elsewhere near the main emission found for ALESS070.1, the χ^2 difference criterion rule them out because they would not fit very well as a Gaussian profile making the continuum fitting the best choice, so the Gaussian fit is not reliable.

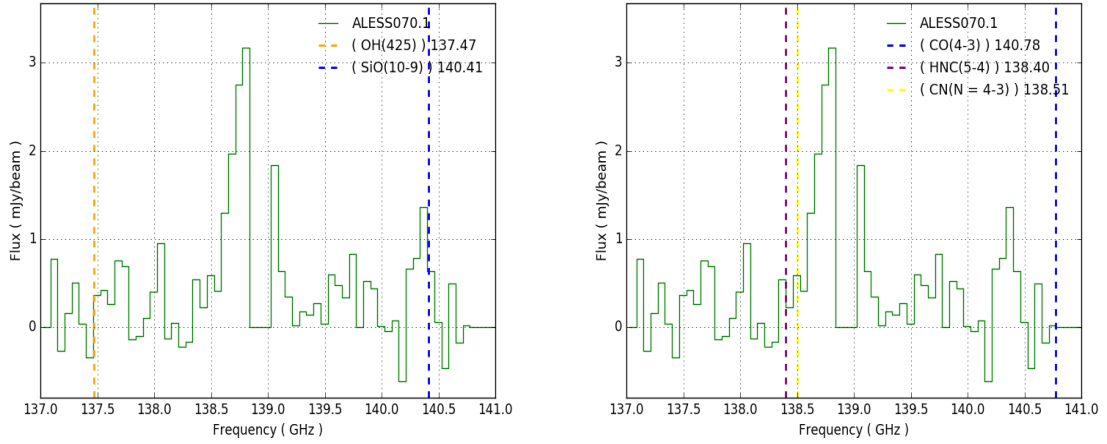


Figure 16: ALESS070.1 spectrum with possible molecule transition from (Spilker et al, 2014). *left*: possible transitions using the spectroscopic redshift. *right*: possible molecule transitions using the photometric redshift. Both redshifts as reported by (Danielson et al, 2017)

In Figure 16, we present the possible emission lines for ALESS070.1 using the spectroscopic redshift (*left*) and photometric redshift (*right*). In the case of the spectroscopic redshift both transitions OH(425) and SiO(10-9) lie aside the central emission and both are not pretty common to be found in this type of galaxies in comparison to CO-transitions. So if this redshift is correct, the expected molecule transitions do not match the current data and we cannot say anything about the line. However, using the photometric redshift we have three new possibilities which corresponds to CO(4-3), HNC(5-4) and CN(4-3). Here, if this was the case, we expect the line to be CO(4-3) because is brighter and more likely to be present compared to the other ones. Based on this, and on the mean frequency obtained through the Gaussian fit in sub-section 3.3.2 we potentially think that this transition corresponds to carbon monoxide.

As an illustration, in Figure 17 we have the redshift versus the observed frequency for the ALMA band4. The grey band represent the whole band4 while the small colored bands show the 4 spectral windows we have in the observations as selected by Dr. Elisabete da Cunha the PI of these data. The different curves show how the observed frequency for a given molecule transition changes with redshift and its most-likely position expected to be observed in the ALMA band4. These curves were obtained with Equation 3.1 where the emission frequency adopted was the same as in (Spilker et al, 2014) for a given transition. Both targets ALESS070.1 and ALESS122.1

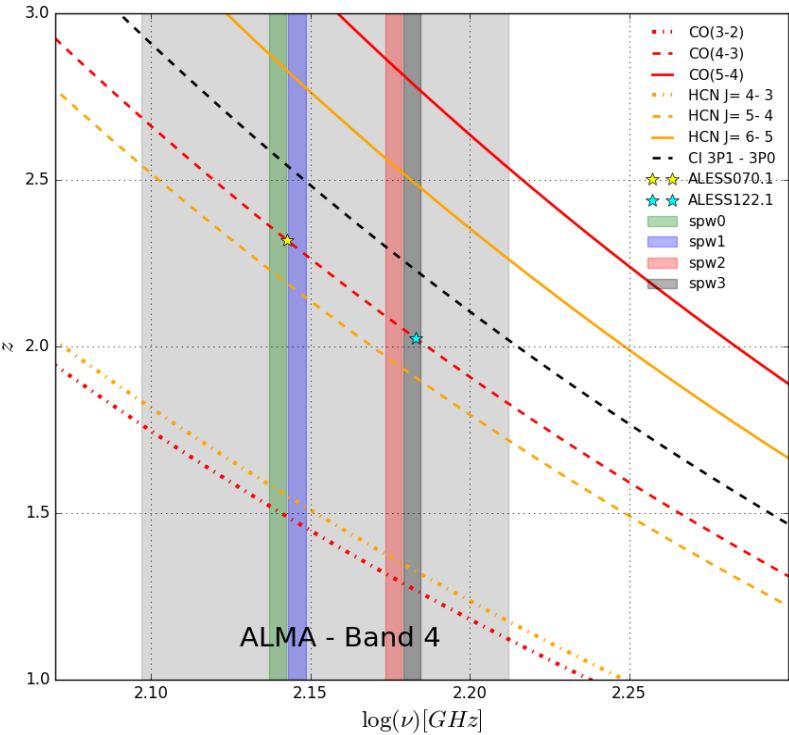


Figure 17: Different molecule transitions expected in the ALMA band4 for a few common molecules. The grey band shows the whole range in frequency covered in band4, whilst the green, purple, red and dark-grey show the four spectral windows used in our observed-data. Both, ALESS070.1 and ALESS122.1 are shown in the position expected through the line fitting obtained above (i.e redshift and observed mean frequency). A few possible transitions for CO, HCN and [CI] are shown in order to illustrate how different redshifts for a given spectral window can lead to different expected emission lines.

are shown as little stars using the redshift found through our analysis. As we have said before, ALESS122.1 matches perfectly the CO-transition ($4 \rightarrow 3$) as can be seen. Although for ALESS070.1 we have adopted the redshift found by the fit assuming the same transition, we can clearly see that the line emission characterization strongly depends on the quality of the measured redshift for the source. One can wrongly characterize an emission line because transitions of different molecules at a given frequency can be observed in the same spectral window depending on redshift. Nevertheless, taking into account all the arguments exposed above, we expect any other molecule transition to be less intense than a CO-emission if present. Additional observation in a different band could definitely proof if the redshift found here either corresponds to the correct one or it is between the upper/lower limits.

3.4 IMAGING: CONTINUUM, LINE AND IR COUNTERPART

We want to know how reliable are our detections, so, in order to do this we imaged ALESS070.1 and ALESS122.1. We will build three different images. The first image corresponds to the continuum+line at the same time, second one just the continuum and the third one just the line. In [Figure 18](#) and [Figure 19](#) we show these images for ALESS070.1 and ALESS122.1 respectively. First of all, the red dot in both cases correspond to the position of the source according to ([Hodge et](#)

al, 2013) and also the place were the spectrum was taken as mentioned before because at least for these two sources it matches perfectly. The Continuum+Line image is generated without performing any primary beam correction and it clearly shows a detection $> 7\sigma$ for both sources. To generate the Continuum we just used those channels where there is absence of line, obtaining a 5σ and 7σ detection for ALESS070.1 and ALESS122.1 respectively. Also to make the line imaging, we only used those channels where there is line and also subtracted the continuum. In this case we obtained a 7σ and 14σ detection for each source respectively. This was all carried out using CASA (McMullin et al, 2007).

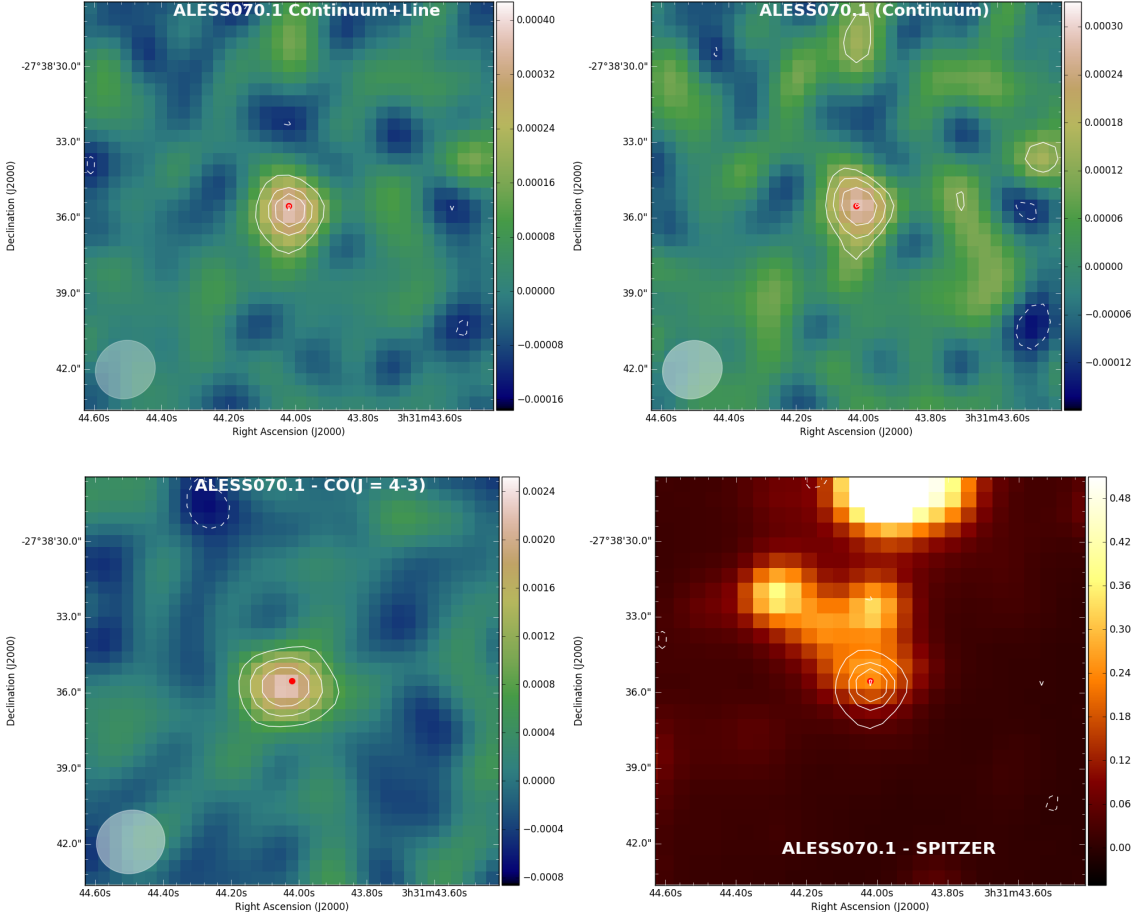


Figure 18: ALESS070.1 imaging. From left-to-right and top-to-bottom, Continuum+Line, Continuum, Line and Spitzer/IRAC images. The contours for the Continuum+Line correspond to $(-2, 3, 4, 5, 7, \dots) \times \text{rms}$ which is equal to $52.8\mu\text{Jy}$. For the Continuum, we show the $(-3, -2, 2, 3, 4, 5) \times \text{rms}$ which is equal to $56.3\mu\text{Jy}$. For the Line CO(4-3) transition we show the $(-5, -3, -2, 3, 5, 7) \times \text{rms}$ which is equal to $247\mu\text{Jy}$. For the SPITZER/IRAC counterpart (Lacy et al, 2005) we over plot the Continuum+Line contours. The red dot shows the position where the spectrum was taken and also the coordinates where the source is centred. The beam size is shown in the left-corner. The color band stands for the flux intensity.

The right-bottom image in Figure 18 and Figure 19 correspond to the SPITZER/IRAC infra-red counterpart (Lacy et al, 2005) just to double check that the source is real and matches the radio observation. This image was obtained combining the $3.6\mu\text{m}$, $4.5\mu\text{m}$, $5.8\mu\text{m}$ and $8\mu\text{m}$ channel of the IRAS camera in *Spitzer* (Fazio et al, 2004). As expected from Figure 14 in both cases, the line is clearly detected with a high signal-to-noise above the continuum emission which is directly related to the high value in the χ^2 difference or the goodness of fit for the Gaussian. The white

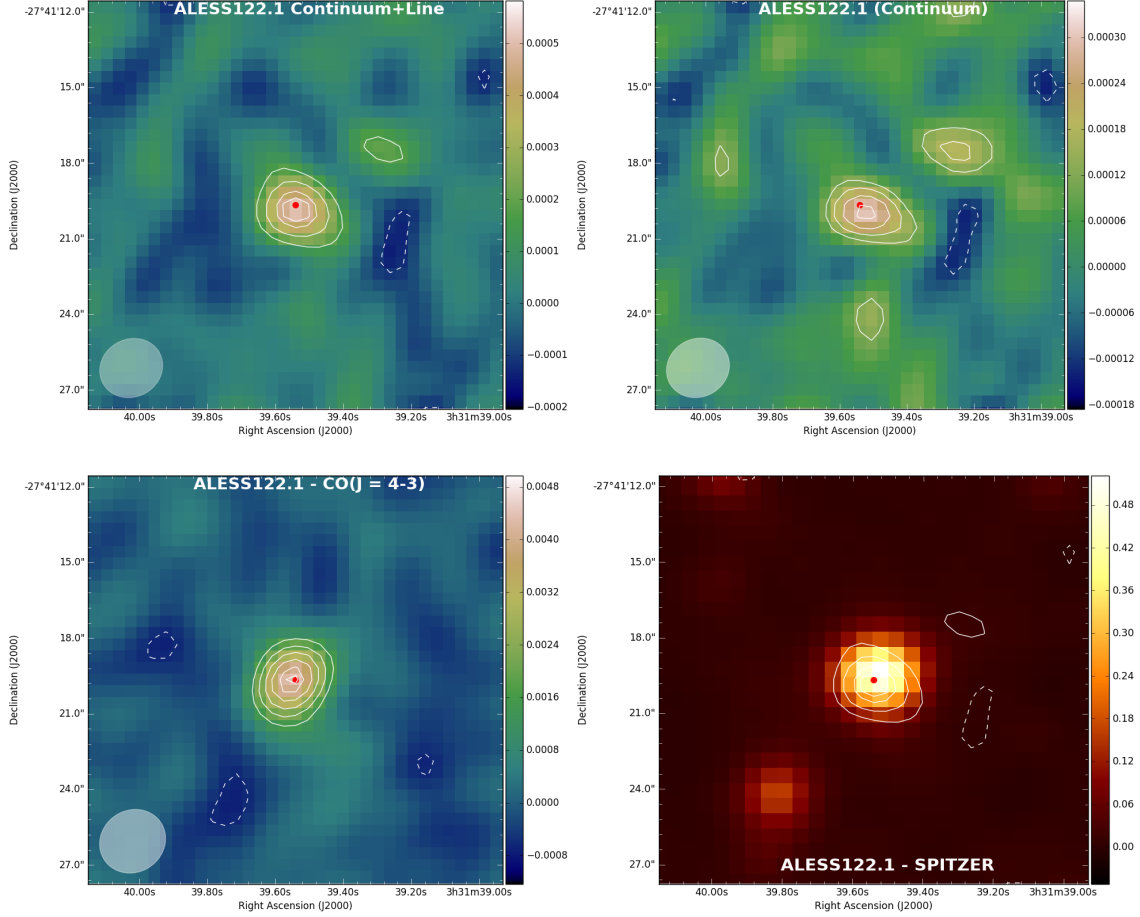


Figure 19: ALESS122.1 imaging. From left-to-right and top-to-bottom, Continuum+Line, Continuum, Line and Spitzer/IRAC images. The contours for the Continuum+Line correspond to $(-2, 3, 4, 5, 7, \dots) \times \text{rms}$ which is equal to $57.3\mu\text{Jy}$. For the Continuum, we show the $(-3, -2, 2, 3, 4, 5, 7) \times \text{rms}$ which is equal to $57.6\mu\text{Jy}$. For the Line CO($J=4-3$) transition we show the $(-5, -3, -2, 5, 7, 9, 11, 13, 14) \times \text{rms}$ which is equal to $306\mu\text{Jy}$. For the SPITZER/IRAC (Lacy et al, 2005) counterpart we over plot the Continuum+Line contours. The red dot shows the position where the spectrum was taken and also the coordinates where the source is centred. The beam size is shown in the left-corner. The color band stands for the flux intensity.

contour here represent the emission line detection of CO($4-3$) for $(-5, -3, -2, 3, 5, 7) \times \text{rms}$.

Next chapters will focus on the derived properties from molecule transitions, specially on the CO transition which will pave the road to all the future physical characterization of these sources applying all the concepts explained in [Chapter 1](#). We compute different parameters as the CO luminosity, the molecular mass, line luminosities, dynamical mass among others to properly characterize our final detections.

RESULTS AND DISCUSSION

4.1 INTRODUCTION

In this chapter different properties as the CO-luminosity, molecular mass, dynamical mass among others are presented for ALESS070.1 and ALESS122.1 obtained through a spectral analysis of CO emission. All the values were obtained analysing the CO(4-3) vibrational transition detected in our ALMA-band 4 observations, as explained in [Chapter 3](#). We also show the SLED for ALESS122.1 including our new measurement, in order to compare it to standard SMGs found in literature and describe the gas properties. An estimation of the CO excitation ladder parameters or CO luminosity ratios r_{31} and r_{41} was computed and compared to reported values in literature. A discussion and future work sections are also included.

4.2 CO LUMINOSITY AND MOLECULAR MASS

As was presented in [Chapter 1, sub-section 1.4.1.1](#) we can obtain the CO-luminosity using [Equation 1.3](#) with every variable in the appropriate units to properly obtain the CO-luminosity in $\text{K km s}^{-1} \text{ pc}^2$ which are the regular units reported in the literature and help us to compare our values with any other data. The redshift we will use is the one obtained through the Gaussian fitting which corresponds to the CO($4 \rightarrow 3$) transition, and the observed frequency to the mean frequency. The integrated line intensity $S_{\text{CO}} \Delta v$ were computed using the FWHM of each emission line properly converted to units of km s^{-1} using [Equation 3.7](#). The distance luminosity was obtained for every source applying [Equation 4.1](#) as presented in ([Hogg et al, 1999](#)),

$$D_L = \int_0^z \frac{c}{H_0} \frac{dz'}{\sqrt{\Omega_m(1+z)^3 + \Omega_\Lambda}} \quad (4.1)$$

where the cosmological parameters H_0 , Ω_m and Ω_Λ were chosen for a flat universe cosmology ($\Omega_k = 0$) as presented in [Chapter 1, sub-section 1.4.1.1](#). Luminosity distance was obtained using *python* numerical integration to solve [Equation 4.1](#) and also double checked with a cosmology calculator available on-line developed by ([Wright et al, 2006](#)). Both methods led to the same results. The different parameters used to compute the CO-luminosity are shown in [Table 5](#).

The luminosity showed in [Table 5](#) corresponds to a luminosity inferred through the CO($4 \rightarrow 3$) transition and we need to link it somehow with the molecular gas mass. However, if we want to use [Equation 1.4](#) we need to convert this value to an equivalent CO($1 \rightarrow 0$) which is the actual transition which traces the molecular gas. In order to do this we have to use a correction factor for the CO-ladder. Therefore, [Equation 1.4](#) can be written in general as (see [Decarli et al, 2016](#)),

$$\frac{M(H_2)}{M_\odot} = \frac{\alpha_{\text{CO}}}{r_{J1}} \frac{L'_{\text{CO}[J-[J-1]]}}{\text{K km s}^{-1} \text{ pc}^2} \quad (4.2)$$

Table 5: Properties computed for ALESS070.1 and ALESS122.1 in order to obtain the CO-luminosity. The units used are shown next to each quantity. Also the propagated uncertainties are presented.

	ALESS070.1	ALESS122.1
$z_{\text{CO}(4-3)}$	2.3197	2.0252
D_L	18623.8	15780.1
$\nu_{\text{obs}} (\text{GHz})$	138.88 ± 0.02	152.44 ± 0.01
$S_{\text{CO}} \Delta v (\text{Jy km s}^{-1})$	2.28 ± 0.48	3.34 ± 0.41
$L'_{\text{CO}(4-3)} (10^{10} \text{ K km s}^{-1} \text{ pc}^2)$	3.64 ± 0.77	4.20 ± 0.52

in [Equation 4.2](#) the term $L'_{\text{CO}[J-J-1]} / r_{J1}$ is called the equivalent CO($1 \rightarrow 0$) luminosity and it is expressed as $L'_{\text{CO}(1-0)}$. In our case $J = 4$, so the correction factor to transform between luminosities which will be used is $r_{41} = 0.31 \pm 0.06$ which was computed by ([Decarli et al, 2016](#)) performing an extrapolation of the values for r_{31} and r_{51} measured by ([Daddi et al, 2015](#)). In [Table 6](#) the molecular mass computed through the CO($1 \rightarrow 0$) luminosity using [Equation 4.2](#) is presented leaving the α_{CO} conversion factor as a free parameter which can be freely choose depending on the type of source due to the big discrepancies in literature.

Table 6: Properties computed for ALESS070.1 and ALESS122.1 in order to obtain the CO($1 \rightarrow 0$) equivalent luminosity and molecular mass $M(\text{H}_2)$ for ALESS070.1 and ALESS122.1

	ALESS070.1	ALESS122.1
$L'_{\text{CO}(1-0)} (10^{10} \text{ K km s}^{-1} \text{ pc}^2)$	11.74 ± 4.76	13.56 ± 4.29
$M(\text{H}_2) (10^{10} M_\odot \alpha_{\text{CO}})$	11.74 ± 4.76	13.56 ± 4.29

For ALESS122.1 the values found for the molecular mass and the equivalent luminosity are in agreement with those reported by ([Huynh et al, 2017](#)), which corresponds to $(13 \pm 2) \times 10^{10} \text{ K km s}^{-1} \text{ pc}^2$ and $(13 \pm 2) \times 10^{10} M_\odot$, respectively. However, we must take into account that their work was performed using CO($1 \rightarrow 0$) transition which is not strongly affected by the conversion factors α_{CO} e.g is less biased.

As was presented in [Chapter 1](#) from [Equation 1.5](#) and [Equation 1.7](#), we can obtain the dynamical mass once the molecular gas mass and line luminosity are measured as presented by ([Solomon & Vanden Bout, 2005](#)) or through the virial estimator as presented by ([Tacconi et al, 2008](#)). The last one is widely used in recent works. However, in the first case the final mass will depend on the CO-to-H₂ conversion factor, while for the other one will depend on the half-light radius. We did not measured any of these values so our results will depend on them. The one-dimensional velocity dispersion is shown in [Table 4](#) and the line luminosity and molecular mass are shown in [Table 5](#) for both ALESS070.1 and ALESS122.1 sources. The values obtained after replacing values in the right units in equations mentioned above are summarized in [Table 7](#).

More observations in order to resolve these sources and measure the half-light radius or a more extensive analysis is needed in order to compute the right numbers corresponding to the dynamical mass. In the next section we discuss the implications of our new data on the CO SLED of ALESS122.1 and derived values for the CO luminosity ratios r_{31} and r_{41} .

Table 7: Dynamical mass computed for ALESS070.1 and ALESS122.1 using the method proposed by (Solomon & Vanden Bout, 2005) to obtain M_{dyn} and (Taconni et al, 2008) $M_{\text{dyn,disk}}$. The errors are not shown because the values are just an estimation that will be finally known after measuring the half-light radius or the proper α_{CO} conversion factor for each source.

	ALESS070.1	ALESS122.1
$M_{\text{dyn}} (10^{10} \alpha_{\text{CO}}^2 M_{\odot})$	~ 11.74	~ 13.56
$M_{\text{dyn,disk}} (10^{10} R_{1/2} [\text{kpc}] M_{\odot})$	~ 3.45	~ 2.31

4.3 SLED FOR ALESS122.1

As was shown in previous sections, we were able to measure the line intensity of the CO(4 → 3) transition for ALESS122.1. However, this source has been studied recently by (Huynh et al, 2017) and (Calistro Rivera et al, 2017b) finding CO(1 → 0) and CO(3 → 2) transitions respectively. Therefore, we can start thinking about the CO spectral line energy distribution (SLED) for this source, though we must have in mind that more observations are needed to obtain higher 'J' transitions. In Figure 20, we present the three available points (in black) for the CO SLED of ALESS122.1. Also, the moderately excited CO SLED of Arp 220 (in yellow) and GN20 (in red) which are standard SMGs to compare with and which values were taken from (Rosenberg et al, 2015) and (Daddi et al, 2009a) respectively as shown. We can start modelling the CO SLED for our source following radiative transfer calculations and large velocity gradient models. However, as we only have three points it is quite hard to obtain a good fit which really constrains the kinetic temperature T_k and the molecular gas density $\rho(H_2)$ due to the lack of high 'J' transitions (Strandet et al, 2017). This is why we decided to overplot the SLED of two well studied sources, in order to properly infer or at least have some initial prior of the behaviour for the ALES122.1 CO SLED to later perform a fit with good initial conditions once more transitions are shown.

Even if we did not apply the solutions for the radiative transfer calculations to our data, we briefly describe the background to understand how our method helps us to shed a light on the behaviour of the gas reservoir. When applying a given model to find the best parameters that fit our CO SLED we basically need to set the background radiation (CMB) plus the dust radiation field. It is also necessary to provide the chemical parameters as the CO abundance relative to the molecular gas which is commonly set to $\sim 8 \times 10^{-5}$ (Strandet et al, 2017) and the absorption efficiency which depends on the frequency. An estimate of collision rates (Carilli et al, 2010) is also needed. Once this is provided, a standard program will solve the equations creating a grid with different parameters varying the kinetic temperature and the column density in order to sample the whole parameter space. Then, it will get the best fit to the data retrieving the line intensity for a given transition and the kinetic temperature which can be translated into line integrated intensity just by multiplying by the FWHM of the line one is measuring. These values need to be interpolated to finally compare them with the actual discrete detections.

As we have re-normalized the CO SLED of Arp 220 and GN20 to the CO (1-0) transition of ALESS122.1 because is less biased and is a better tracer of the molecular mass, we can barely infer the physics of our gas just comparing with them as a first approximation. In (Carilli et al, 2010), GN20 was studied and fitted with two components, one for the lower transitions and another one for the higher transitions. The lower excitation fit led to a kinetic temperature of $\sim 30\text{K}$ and molecular density of $\sim 300\text{cm}^{-3}$ while for the high excitation component they obtained $\sim 45\text{K}$

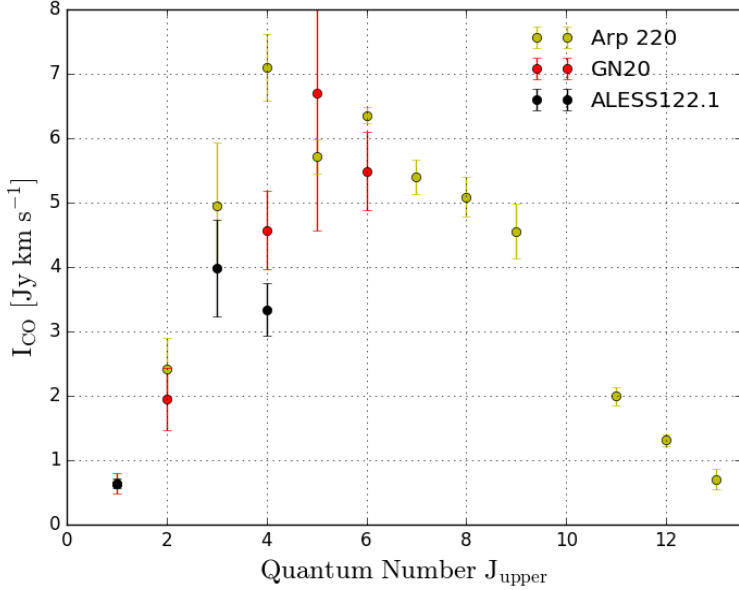


Figure 20: Results for the CO SLED (Spectral Line Energy Distribution) of ALESS122.1. The *x*-axis corresponds to the upper J transition and the *y*-axis to the integrated intensity I_{CO} given in Jy km s^{-1} . The black dots correspond to measurements performed by (Huynh et al, 2017) for $\text{CO}(1 \rightarrow 0)$, (Calistro Rivera et al, 2017b) in prep. for $\text{CO}(3 \rightarrow 2)$ and our observation for $\text{CO}(4 \rightarrow 3)$. The yellow and red dots corresponds to very well known SLEDS of Arp220 (Rosenberg et al, 2015) and GN20 (Carilli et al, 2010). The first three transition for Arp220 were measured by (Greve et al, 2009). The transition $\text{CO}(4 \rightarrow 3)$ for GN20 was measured by (Daddi et al, 2009a). Both Arp220 and GN20 SLEDS were normalized to the $\text{CO}(1\text{-}0)$ transition of ALESS122.1 to properly compare.

and $\sim 6300\text{cm}^{-3}$. In this case, higher excitation component is understood as transition above $\text{CO}(3 \rightarrow 2)$ which represents the compact component of the gas, while those below this limit represent the extended component i.e. the full molecular gas reservoir (Carilli et al, 2010). On the other hand for Arp 220, the values found in literature correspond to a kinetic temperature of $\sim 180\text{K}$ and a molecular density of $\sim 10^5\text{cm}^{-3}$. As we can observe in Figure 20, our observations are pretty much below the excited CO SLED for Arp 220 and closer to the trend of GN20. Additionally, as we only have transitions up to $\text{CO}(4 \rightarrow 3)$, at the moment we could only be able to study the extended component of the molecular gas. Hence, we could say that ALESS122.1 CO SLED will have eventually if more measurements are performed, a kinetic temperature around 30K and a molecular gas density of $\sim 300\text{cm}^{-3}$ for the full molecular gas reservoir. However, we must take this with caution because until we fit the final CO SLED we will not be totally sure whether our estimates are the right ones or not. This method carries to the gas mass estimate, which is useful in order to compare to the values obtained through our spectral analysis in Table 6 and finally constrain the real value of the CO-to-H₂ conversion factor which is often set to $\alpha_{CO} = 0.8 \text{ M}_\odot (\text{K km s}^{-1} \text{ pc}^2)^{-1}$ because it is consistent with the center of ULIRGs as shown by (Downes & Solomon, 1998).

$$r_{j1,j2} = \frac{I_{CO(j1,j1-1)}}{I_{CO(j2,j2-1)}} \left(\frac{j2}{j1} \right)^2 \quad (4.3)$$

On the other hand using ALESS122.1 we can compute the CO luminosity ratios as we have three integrated line luminosities including our measurement. As it is presented in (Daddi et

al, 2015) we can obtain them through [Equation 4.3](#). This is equivalent to the brightness temperature ratios between luminosities j_1 and j_2 only in the limit of small Rayleigh-Jeans corrections. Using $I_{CO(3-2)} = 3.99 \pm 0.75$ Jy km s $^{-1}$ reported by ([Calistro Rivera et al, 2017b](#)) and $I_{CO(1-0)} = 0.64 \pm 0.07$ Jy km s $^{-1}$ reported by ([Huynh et al, 2017](#)) we obtain $r_{31} = 0.69 \pm 0.02$. Using our value for the CO(4 \rightarrow 3) transition as shown in [Table 6](#) and the same value used above for the CO(1 \rightarrow 0) we obtain $r_{41} = 0.32 \pm 0.01$. Our result for r_{41} is in total agreement with values reported by ([Daddi et al, 2015](#)) and adopted in recent works as ([Decarli et al, 2016](#)). However, for r_{31} the value differs in $\sim 60\%$ with that reported in ([Daddi et al, 2015](#)) because the integrated line luminosity is larger for that transition in our source (see [Figure 20](#)) making the CO luminosity ratio larger as well. We need higher 'J' transitions to better constrain the maximum of our CO SLED and finally explain the value found for r_{31} . The same exercise can be perform by assuming the α_{CO} parameter in [Equation 1.4](#) equal to all the transitions, the molecular mass equal to the one reported by ([Huynh et al, 2017](#)) for the CO(1 \rightarrow 0) and replacing the measured line luminosity. This leads quite to the same results, of course not as precise as using the above equation because we are making a few assumptions. However it was used to double check.

In the next section, we address a final discussion about the overall work, the main results and its implications for the actual research of SMGs. We also present some future ideas that could be developed in order to check our results and finally constrain the properties for ALESS sources.

4.4 DISCUSSION

We have analyzed a sample of 51 ALESS targets in order to search for emission lines present in the ALMA-band 4 observations. As was shown above, we only clearly detected two CO emission which satisfied all the requirements imposed in order to guarantee real detections. It is likely that some of our possible candidates rejected were real, but until having more observations we can not really use them as they are just barely above the signal-to-noise criterion. We must have in mind that a few lines could also be present in our data but due to the observation set-up they are not too strong, also because the observations were not designed to target a given molecule transition, or sensitivity of our instruments. A way to improve our detections is a method known as 'stacking'. However, we have no sufficient data to perform this, but it is something that we could have in mind for future observations.

Most of our results are derived from the CO(4 \rightarrow 3) transition. As was exposed above, this is not the real tracer of molecular gas mass, then we need to apply a few corrections to convert our line luminosity into an equivalent luminosity for CO(1 \rightarrow 0) which is less biased and is the real tracer of m_{H_2} . The line intensity will be subject to the integrated line width, which in our case was chosen to be the FWHM of the given line to properly match it to the $\Delta_{v,FWHM}$ in [Equation 1.7](#).

ALESS122.1 shows a really prominent transition line which is highly above the continuum and satisfies the $\Delta\chi^2$ -difference without any problem. In the case of ALESS070.1, we have the transition line in between the 'spw0' and 'spw1' which can be seen as a gap in the emission line (see [Figure 14](#)). Although this represents a problem because we are not getting all the information for the line, the line is bright enough to be above the continuum and achieve the needed $\Delta\chi^2$ -difference to be accepted. However, the detection of the line can be improved with a complete observation of the line, obtaining better values to the one-dimensional velocity dispersion that

basically improves the way we obtain the molecular mass and line luminosity.

These transitions represent a crucial way to measure the spectroscopic redshift of the sources and constrain the parameters that describe the ongoing physics in the gas reservoirs. ALESS122.1 has been studied before by (Huynh et al, 2017) using CO(1 → 0) and by (Calistro Rivera et al, 2017b) through CO(3 → 2). As we only have transitions up to CO(4 → 3), we see the extended emission which is consistent to the full amount of molecular gas in the galaxy, but we have no information about the compact regions which need higher 'J' transitions. Our measurements represent new extra information to compare with, at least for the molecular and dynamical masses, and a contribution to the CO SLED. This also represents a way to properly calibrate the r_{31} and r_{41} luminosity ratios by comparing different transitions which in the case of ALESS122.1 turn out to be close to values reported in literature at least for our CO(4 → 3) detection. On the other hand, the detection for ALESS070.1 adds totally brand new and valuable information to study the physical conditions of the gas as to constrain the molecular mass and for future CO studies.

Our results were obtained for CO(4 → 3) transitions in the ALMA-band 4. These objects were not resolved, so we cannot perform any deep study about the dynamics of the gas, the rotational gradient, temperature gradient, size of the disk among others. New observations in different bands to obtain any other transition expected to the actual measured redshifts or just to simply resolve the source and perform a dynamical study of the sources is needed. Different ideas which could be addressed and explored in the future are explained in the next section.

4.5 FUTURE WORK

In this project, we have detected two CO transitions in two ALESS sources. However, as we have not only ALESS sources in each observation but also nearby objects, we can think about performing a blind search to obtain any kind of emission lines present in each image. This can lead to multiple information of the emission lines which are useful to perform the stacking analysis. Additionally, new measurements in different bands are needed to confirm our results for ALESS070.1 and to add more valuable data to the ALESS sources. As was mentioned before, this data represents ALMA-band 4 observations obtained as part of a project by the PI. Dr. Elisabete da Cunha. However, a new observational proposal proposed by the same PI. to target [CII]-emission in ALMA-band 9 will shed light about the results we present here to confirm the spectroscopic redshift. Obtaining resolved data is also important in order to study the dynamics and the properties of the disks which can be combined with galactic models to deeply study this SMG population. As more observations are performed, more data points are added to the SLED for a given molecule. This implies that we can fit the SLED to the radiative transfer models in order to study the extended or compact emission in the reservoirs, the temperature and density gradients of the gas among others. Measuring the redshift through this technique needs less observation time, so we can specifically target a given emission and survey the ALESS sources using as prior the redshifts available for them to verify the redshifts measured in the zLESS project.

SUMMARY

We have presented a study of two CO observations to derive properties of sources catalogued in the ALESS-survey. Our ALMA observations were performed in the *Band-4* (C36-1 configuration) using a frequency range from 137 GHz to 153 GHz, where every target was observed for 40 seconds reaching a rms of $52.6 \mu\text{Jy}/\text{beam}$ allowing us to precisely study any emission line present in those sources. Although, the project was not dedicated to study line emission but dust continuum, we obtain free 3D data which can be used to search for line emission in our bandwidth. Because of this, if any line present we must be quite sure of its distance in order to characterize the line, otherwise it would lead to misclassification and wrong physical properties interpretation.

We detected a CO($4 \rightarrow 3$) transition in two out of 51 sources, corresponding to ALESS070.1 and ALESS122.1. In the case of ALESS122.1 multiple studies have been carried out to study CO transitions as have been reported in literature by (Huynh et al, 2017, Calistro Rivera et al, 2017b) and also optic spectrum analysis in order to obtain well-measured redshifts (Danielson et al, 2017). The molecular mass ($M_{\text{H}_2} = (13.56 \pm 4.29) 10^{10} M_{\odot} \alpha_{\text{CO}}$) and redshift ($z \sim 2.0252$) obtained for ALESS122.1 through our spectroscopic analysis is in well agreement with previous values reported by (Huynh et al, 2017). Our detection represents new data for the CO SLED which helps us to understand the conditions of the molecular gas (i.e. the full amount of gas because we are looking to the extended emission) environment for later study the dynamics. However, we need more measurements to properly fit the CO SLED to obtain the temperature and density of the gas. Also different observations to resolve this object is needed if one wants to study the dynamics, because in our case as was checked it is not resolved, so we cannot perform a good study of the gas.

On the other hand, the line detection for ALESS070.1 is in between the gap produced by two spectral windows which depends on the way the PI performs the observation. Although, this basically affects the quality of the derived line luminosity and later the molecular mass values, the signal-to-noise ratio is high enough to trust this emission as a real one. We performed different experiments to double check which emission line it could be due to the fact that the spectroscopic redshift reported by (Danielson et al, 2017) does not match any plausible emission line present in this range. However, the known photometric redshift does not matches perfectly the emission, though it gives us a clue of which kind of molecule transition could be, turning out to be a CO($4 \rightarrow 3$) after an extensive analysis. New observations in different bands targeting possible emission lines present are needed to finally confirm this redshift and start filling the CO SLED for this source. The computed molecular mass and redshift for this source corresponds to $M_{\text{H}_2} = (11.74 \pm 4.76) 10^{10} M_{\odot} \alpha_{\text{CO}}$ and $z \sim 2.3197$.

The conversion factor α_{CO} was left as a free parameter because at the moment different values are reported in the literature spanning in a wide range. However, we can start thinking about the possible values for ALESS122.1 because as we have three different transitions measured for CO,

we could eventually compute it to obtain the final values for molecular and dynamical mass for both sources. In both cases we computed the dynamical mass, however, it was left in terms of the CO-to-H₂ conversion factor or the half light radius. Future observations are needed to obtain the size of the sources in order to properly study the dynamics of the gas because with our current observations the sources resulted be not resolved after deconvolving the beam. The values obtained for ALESS122.1 after comparing our emission CO(4 → 3) and ([Calistro Rivera et al, 2017b](#)) CO(3 → 2) to ([Huynh et al, 2017](#)) CO(1 → 0) correspond to $r_{31} = 0.69 \pm 0.02$ and $r_{41} = 0.32 \pm 0.01$. This is in agreement with values reported and widely used in literature for our CO(4 → 3) detection.

In the future, targeting a given molecule transition for ALESS sources could be addressed using as priors the redshifts provided by the zLESS project ([Danielson et al, 2017](#)). Also, analysing our current data in search for any emission line present not only in the ALESS source but in any source in the field could be really interesting.

BIBLIOGRAPHY

- [1] A. D. Biggs, R. J. Ivison, E. Ibar, J. L. Wardlow, H. Dannerbauer, I. Smail, F. Walter, A. Weiß, S. C. Chapman, K. E. K. Coppin, C. De Breuck, M. Dickinson, K. K. Knudsen, V. Mainieri, K. Menten, and C. Papovich. The LABOCA survey of the Extended Chandra Deep Field-South - radio and mid-infrared counterparts to submillimetre galaxies. *Monthly Notices of the Royal Astronomical Society*, 413:2314–2338, Jun 2011. (Cited on pages 3, 10, and 12.)
- [2] A. W. Blain, R. J. Ivison, J.-P. Kneib, and I. Smail. Galaxy counts at $450\text{ }\mu\text{m}$ and $850\text{ }\mu\text{m}$. 193: 246, 1999b. (Cited on page 1.)
- [3] A. W. Blain, I. Smail, R. J. Ivison, J.-P. Kneib, and D. T. Frayer. Submillimeter galaxies. *Physics Reports*, 369:111–176, Oct 2002. (Cited on pages 1, 2, 3, 4, and 5.)
- [4] G Calistro-Rivera. *in prep.*, 2017b. (Cited on pages x, 37, 38, 39, 40, 41, and 42.)
- [5] C. L. Carilli and F. Walter. Cool Gas in High-Redshift Galaxies. *Annual Review of Astron and Astrophys*, 51:105–161, Aug 2013. (Cited on page 6.)
- [6] C. L. Carilli, E. Daddi, D. Riechers, F. Walter, A. Weiss, H. Dannerbauer, G. E. Morrison, J. Wagg, R. Davé, D. Elbaz, D. Stern, M. Dickinson, M. Krips, and M. Aravena. Imaging the Molecular Gas in a Submillimeter Galaxy at $z = 4.05$: Cold Mode Accretion or a Major Merger? *Astrophysical Journal*, 714:1407–1417, May 2010. (Cited on pages x, 37, and 38.)
- [7] C. L. Carilli, J. Chluba, R. Decarli, F. Walter, M. Aravena, J. Wagg, G. Popping, P. Cortes, J. Hodge, A. Weiß, F. Bertoldi, and D. Riechers. The ALMA Spectroscopic Survey in the Hubble Ultra Deep Field: Implications for Spectral Line Intensity Mapping at Millimeter Wavelengths and CMB Spectral Distortions. *Astrophysical Journal*, 833:73, Dec 2016. (Cited on page 9.)
- [8] C. M. Casey, D. Narayanan, and A. Cooray. Dusty star-forming galaxies at high redshift. *Physics Reports*, 541:45–161, Aug 2014. (Cited on pages viii, 2, 3, 5, 7, and 8.)
- [9] F. Combes. Molecular Gas in High Redshift Galaxies. *Astronomical Society of the Pacific Conference Series*, 476:23, Oct 2013. (Cited on page 10.)
- [10] E. da Cunha, B. Groves, F. Walter, R. Decarli, A. Weiß, F. Bertoldi, C. Carilli, E. Daddi, D. Elbaz, R. Ivison, R. Maiolino, D. Riechers, H.-W. Rix, M. Sargent, and I. Smail. On the Effect of the Cosmic Microwave Background in High-redshift (Sub-)millimeter Observations. *Astrophysical Journal*, 766:13, Mar 2013. (Cited on page 4.)
- [11] E. Daddi, H. Dannerbauer, D. Stern, M. Dickinson, G. Morrison, D. Elbaz, M. Giavalisco, C. Mancini, A. Pope, and H. Spinrad. Two Bright Submillimeter Galaxies in a $z = 4.05$ Protocluster in GOODS-North, and Accurate Radio-Infrared Photometric Redshifts. *Astrophysical Journal*, 694:1517–1538, Apr 2009a. (Cited on pages x, 37, and 38.)
- [12] E. Daddi, H. Dannerbauer, D. Liu, M. Aravena, F. Bournaud, F. Walter, D. Riechers, G. Magdis, M. Sargent, M. Béthermin, C. Carilli, A. Cibinel, M. Dickinson, D. Elbaz, Y. Gao, R. Gobat,

- J. Hodge, and M. Krips. CO excitation of normal star-forming galaxies out to $z = 1.5$ as regulated by the properties of their interstellar medium. *Astronomy and Astrophysics*, 577: A46, May 2015. (Cited on pages 36 and 39.)
- [13] A. L. R. Danielson, A. M. Swinbank, I. Smail, J. M. Simpson, C. M. Casey, S. C. Chapman, E. da Cunha, J. A. Hodge, F. Walter, J. L. Wardlow, D. M. Alexander, W. N. Brandt, C. de Breuck, K. E. K. Coppin, H. Dannerbauer, M. Dickinson, A. C. Edge, E. Gawiser, R. J. Ivison, A. Karim, A. Kovacs, D. Lutz, K. Menten, E. Schinnerer, A. Weiß, and P. van der Werf. An ALMA Survey of Submillimeter Galaxies in the Extended Chandra Deep Field South: Spectroscopic Redshifts. *Astrophysical Journal*, 840:78, may 2017. (Cited on pages ix, x, 10, 11, 12, 15, 16, 23, 26, 27, 28, 29, 30, 41, and 42.)
- [14] R. Decarli, I. Smail, F. Walter, A. M. Swinbank, S. Chapman, K. E. K. Coppin, P. Cox, H. Dannerbauer, T. R. Greve, J. A. Hodge, R. Ivison, A. Karim, K. K. Knudsen, L. Lindroos, H.-W. Rix, E. Schinnerer, J. M. Simpson, P. van der Werf, and A. Weiß. An ALMA Survey of Sub-millimeter Galaxies in the Extended Chandra Deep Field South: Sub-millimeter Properties of Color-selected Galaxies. *Astrophysical Journal*, 780:115, Jan 2014. (Cited on pages 4 and 11.)
- [15] R. Decarli, F. Walter, M. Aravena, C. Carilli, R. Bouwens, E. da Cunha, E. Daddi, D. Elbaz, D. Riechers, I. Smail, M. Swinbank, A. Weiß, R. Bacon, F. Bauer, E. F. Bell, F. Bertoldi, S. Chapman, L. Colina, P. C. Cortes, P. Cox, J. Gómez-López, H. Inami, R. Ivison, J. Hodge, A. Karim, B. Magnelli, K. Ota, G. Popping, H.-W. Rix, M. Sargent, A. van der Wel, and P. van der Werf. The ALMA Spectroscopic Survey in the Hubble Ultra Deep Field: Molecular Gas Reservoirs in High-redshift Galaxies. *Astrophysical Journal*, 833:70, Dec 2016. (Cited on pages 1, 7, 35, 36, and 39.)
- [16] D. Downes and P. M. Solomon. Rotating Nuclear Rings and Extreme Starbursts in Ultraluminous Galaxies. *Astrophysical Journal*, 507:615–654, Nov 1998. (Cited on page 38.)
- [17] G. G. Fazio, J. L. Hora, L. E. Allen, M. L. N. Ashby, P. Barmby, L. K. Deutsch, J.-S. Huang, S. Kleiner, M. Marengo, S. T. Megeath, G. J. Melnick, M. A. Pahre, B. M. Patten, J. Polizotti, H. A. Smith, R. S. Taylor, Z. Wang, S. P. Willner, W. F. Hoffmann, J. L. Pipher, W. J. Forrest, C. W. McMurry, C. R. McCreight, M. E. McKelvey, R. E. McMurray, D. G. Koch, S. H. Moseley, R. G. Arendt, J. E. Mentzell, C. T. Marx, P. Losch, P. Mayman, W. Eichhorn, D. Krebs, M. Jhabvala, D. Y. Gezari, D. J. Fixsen, J. Flores, K. Shakoorzadeh, R. Jungo, C. Hakun, L. Workman, G. Karpati, R. Kichak, R. Whitley, S. Mann, E. V. Tollestrup, P. Eisenhardt, D. Stern, V. Gorjian, B. Bhattacharya, S. Carey, B. O. Nelson, W. J. Glaccum, M. Lacy, P. J. Lowrance, S. Laine, W. T. Reach, J. A. Stauffer, J. A. Surace, G. Wilson, E. L. Wright, A. Hoffman, G. Domingo, and M. Cohen. The Infrared Array Camera (IRAC) for the Spitzer Space Telescope. *Astrophysical Journal, Supplement*, 154:10–17, Sep 2004. (Cited on page 32.)
- [18] Y. Gao and P. M. Solomon. The Star Formation Rate and Dense Molecular Gas in Galaxies. *Astrophysical Journal*, 606:271–290, May 2004. (Cited on page 9.)
- [19] M. Ginolfi, R. Maiolino, T. Nagao, S. Carniani, F. Belfiore, G. Cresci, B. Hatsukade, F. Mannucci, A. Marconi, A. Pallottini, R. Schneider, and P. Santini. Molecular gas on large circumgalactic scales at $z = 3.47$. *Monthly Notices of the Royal Astronomical Society*, 468:3468–3483, Jul 2017. (Cited on page 6.)

- [20] T. R. Greve, P. P. Papadopoulos, Y. Gao, and S. J. E. Radford. Molecular Gas in Extreme Star-Forming Environments: The Starbursts Arp 220 and NGC 6240 as Case Studies. *Astrophysical Journal, Supplement*, 692:1432–1446, Feb 2009. (Cited on pages [x](#) and [38](#).)
- [21] C. C. Hayward, D. Kereš, P. Jonsson, D. Narayanan, T. J. Cox, and L. Hernquist. What Does a Submillimeter Galaxy Selection Actually Select? The Dependence of Submillimeter Flux Density on Star Formation Rate and Dust Mass. *Astrophysical Journal*, 743:159, Dec 2011. (Cited on page [1](#).)
- [22] J. A. Hodge, A. Karim, I. Smail, A. M. Swinbank, F. Walter, A. D. Biggs, R. J. Ivison, A. Weiß, D. M. Alexander, F. Bertoldi, W. N. Brandt, S. C. Chapman, K. E. K. Coppin, P. Cox, A. L. R. Danielson, H. Dannerbauer, C. De Breuck, R. Decarli, A. C. Edge, T. R. Greve, K. K. Knudsen, K. M. Menten, H.-W. Rix, E. Schinnerer, J. M. Simpson, J. L. Wardlow, and P. van der Werf. An ALMA Survey of Submillimeter Galaxies in the Extended Chandra Deep Field South: Source Catalog and Multiplicity. *Astrophysical Journal*, 768:91, May 2013. (Cited on pages [viii](#), [x](#), [10](#), [11](#), [12](#), [14](#), [15](#), [16](#), [21](#), and [32](#).)
- [23] J. A. Hodge, A. M. Swinbank, J. M. Simpson, I. Smail, F. Walter, D. M. Alexander, F. Bertoldi, A. D. Biggs, W. N. Brandt, S. C. Chapman, C. C. Chen, K. E. K. Coppin, P. Cox, H. Dannerbauer, A. C. Edge, T. R. Greve, R. J. Ivison, A. Karim, K. K. Knudsen, K. M. Menten, H.-W. Rix, E. Schinnerer, J. L. Wardlow, A. Weiß, and P. van der Werf. Kiloparsec-scale Dust Disks in High-redshift Luminous Submillimeter Galaxies. *Astrophysical Journal*, 833:103, Dec 2016. (Cited on page [10](#).)
- [24] D. W. Hogg. Distance measures in cosmology. *ArXiv*, May 1999. (Cited on page [35](#).)
- [25] M. T. Huynh, B. H. C. Emonts, A. E. Kimball, N. Seymour, I. Smail, A. M. Swinbank, W. N. Brandt, C. M. Casey, S. C. Chapman, H. Dannerbauer, J. A. Hodge, R. J. Ivison, E. Schinnerer, A. P. Thomson, P. van der Werf, and J. L. Wardlow. The AT-LESS CO(1-0) survey of submillimetre galaxies in the Extended Chandra Deep Field South: First results on cold molecular gas in galaxies at $z \sim 2$. *Monthly Notices of the Royal Astronomical Society*, 467:1222–1230, May 2017. (Cited on pages [x](#), [6](#), [12](#), [36](#), [37](#), [38](#), [39](#), [40](#), [41](#), and [42](#).)
- [26] S. Iglesias-Groth, A. Díaz-Sánchez, R. Rebolo, and H. Dannerbauer. A near/mid infrared search for ultra-bright submillimetre galaxies: Searching for Cosmic Eyelash Analogues. *Monthly Notices of the Royal Astronomical Society*, 467:330–339, May 2017. (Cited on page [3](#).)
- [27] A. Karim, A. M. Swinbank, J. A. Hodge, I. R. Smail, F. Walter, A. D. Biggs, J. M. Simpson, A. L. R. Danielson, D. M. Alexander, F. Bertoldi, C. de Breuck, S. C. Chapman, K. E. K. Coppin, H. Dannerbauer, A. C. Edge, T. R. Greve, R. J. Ivison, K. K. Knudsen, K. M. Menten, E. Schinnerer, J. L. Wardlow, A. Weiß, and P. van der Werf. An ALMA survey of submillimetre galaxies in the Extended Chandra Deep Field South: high-resolution 870 μm source counts. *Monthly Notices of the Royal Astronomical Society*, 432:2–9, Jun 2013. (Cited on pages [10](#), [11](#), and [12](#).)
- [28] M. Lacy, G. Wilson, F. Masci, L. J. Storrie-Lombardi, P. N. Appleton, L. Armus, S. C. Chapman, P. I. Choi, D. Fadda, F. Fang, D. T. Frayer, I. Heinrichsen, G. Helou, M. Im, S. Laine, F. R. Marleau, D. L. Shupe, B. T. Soifer, G. K. Squires, J. Surace, H. I. Teplitz, and L. Yan. The Infrared Array Camera Component of the Spitzer Space Telescope Extragalactic First Look Survey. *Astrophysical Journal, Supplement*, 161:41–52, Nov 2005. (Cited on pages [ix](#), [x](#), [32](#), and [33](#).)

- [29] R. R. Lindner, A. J. Baker, A. Omont, A. Beelen, F. N. Owen, F. Bertoldi, H. Dole, N. Fiolet, A. I. Harris, R. J. Ivison, C. J. Lonsdale, D. Lutz, and M. Polletta. A Deep 1.2 mm Map of the Lockman Hole North Field. *Astrophysical Journal*, 737:83, Aug 2011. (Cited on page 3.)
- [30] C. J. Lonsdale, D. Farrah, and H. E. Smith. Ultraluminous Infrared Galaxies. *Springer*, page 285, 2006. (Cited on page 1.)
- [31] J. P. McMullin, B. Waters, D. Schiebel, W. Young, and K. Golap. Astronomical Data Analysis Software and Systems XVI. *ASP Conf. Ser.* 376, ed. R. A. Shaw, F. Hill, & D. J. Bell (San Francisco, CA: ASP), 2007. (Cited on page 32.)
- [32] G. Popping, R. Decarli, A. W. S. Man, E. J. Nelson, M. Béthermin, C. De Breuck, V. Mainieri, P. G. van Dokkum, B. Gullberg, E. van Kampen, M. Spaans, and S. C. Trager. ALMA reveals starburst-like interstellar medium conditions in a compact star-forming galaxy at $z \sim 2$ using [CI] and CO. mar 2017. (Cited on page 9.)
- [33] M. J. F. Rosenberg, P. P. van der Werf, S. Aalto, L. Armus, V. Charmandaris, T. Díaz-Santos, A. S. Evans, J. Fischer, Y. Gao, E. González-Alfonso, T. R. Greve, A. I. Harris, C. Henkel, F. P. Israel, K. G. Isaak, C. Kramer, R. Meijerink, D. A. Naylor, D. B. Sanders, H. A. Smith, M. Spaans, L. Spinoglio, G. J. Stacey, I. Veenendaal, S. Veilleux, F. Walter, A. Weiß, M. C. Wiedner, M. H. D. van der Wiel, and E. M. Xilouris. The Herschel Comprehensive (U)LIRG Emission Survey (HERCULES): CO Ladders, Fine Structure Lines, and Neutral Gas Cooling. *Astrophysical Journal, Supplement*, 801:72, Mar 2015. (Cited on pages x, 37, and 38.)
- [34] D. B. Sanders and I. F. Mirabel. Luminous Infrared Galaxies. *Annual Review of Astron and Astrophys*, 34:749, 1996. (Cited on page 1.)
- [35] J. M. Simpson, I. Smail, A. M. Swinbank, S. C. Chapman, J. E. Geach, R. J. Ivison, A. P. Thomson, I. Artxaga, A. W. Blain, W. I. Cowley, C.-C. Chen, K. E. K. Coppin, J. S. Dunlop, A. C. Edge, D. Farrah, E. Ibar, A. Karim, K. K. Knudsen, R. Meijerink, M. J. Michałowski, D. Scott, M. Spaans, and P. P. van der Werf. The SCUBA-2 Cosmology Legacy Survey: ALMA Resolves the Bright-end of the Sub-millimeter Number Counts. *Astrophysical Journal*, 807:128, Jul 2015b. (Cited on page 10.)
- [36] P. M. Solomon and P. A. Vanden Bout. Molecular Gas at High Redshift. *Annual Review of Astron and Astrophys*, 43:677–725, Sep 2005. (Cited on pages x, 6, 7, 8, 9, 10, 36, and 37.)
- [37] P. M. Solomon, S. J. E. Radford, and D. Downes. Molecular gas content of the primaeval galaxy IRAS 10214 + 4724. *Nature*, 356:318, Mar 1992b. (Cited on page 9.)
- [38] J. S. Spilker, D. P. Marrone, J. E. Aguirre, M. Aravena, M. L. N. Ashby, M. Béthermin, C. M. Bradford, M. S. Bothwell, M. Brodwin, J. E. Carlstrom, S. C. Chapman, T. M. Crawford, C. de Breuck, C. D. Fassnacht, A. H. Gonzalez, T. R. Greve, B. Gullberg, Y. Hezaveh, W. L. Holzapfel, K. Husband, J. Ma, M. Malkan, E. J. Murphy, C. L. Reichardt, K. M. Rotermund, B. Stalder, A. A. Stark, M. Strandet, J. D. Vieira, A. Weiß, and N. Welikala. The Rest-frame Submillimeter Spectrum of High-redshift, Dusty, Star-forming Galaxies. *Astrophysical Journal*, 785:149, apr 2014. (Cited on pages ix, x, 22, 23, 29, and 30.)
- [39] M. L. Strandet, A. Weiss, C. De Breuck, D. P. Marrone, J. D. Vieira, M. Aravena, M. L. N. Ashby, M. Béthermin, M. S. Bothwell, C. M. Bradford, J. E. Carlstrom, S. C. Chapman, D. J. M. Cunningham, C.-C. Chen, C. D. Fassnacht, A. H. Gonzalez, T. R. Greve, B. Gullberg, C. C.

- Hayward, Y. Hezaveh, K. Litke, J. Ma, M. Malkan, K. M. Menten, T. Miller, E. J. Murphy, D. Narayanan, K. A. Phadke, K. M. Rotermund, J. S. Spilker, and J. Sreevani. ISM Properties of a Massive Dusty Star-forming Galaxy Discovered at $z \sim 7$. *Astrophysical Journal, letters*, 842:L15, Jun 2017. (Cited on page 37.)
- [40] A. M. Swinbank, A. Karim, I. Smail, J. Hodge, F. Walter, F. Bertoldi, A. D. Biggs, C. de Breuck, S. C. Chapman, K. E. K. Coppin, P. Cox, A. L. R. Danielson, H. Dannerbauer, R. J. Ivison, T. R. Greve, K. K. Knudsen, K. M. Menten, J. M. Simpson, E. Schinnerer, J. L. Wardlow, A. Weiß, and P. van der Werf. An ALMA survey of submillimetre galaxies in the Extended Chandra Deep Field-South: detection of [C II] at $z = 4.4$. *Monthly Notices of the Royal Astronomical Society*, 427:1066–1074, Dec 2012. (Cited on pages ix, 9, 10, 12, and 25.)
- [41] A. M. Swinbank, J. M. Simpson, I. Smail, C. M. Harrison, J. A. Hodge, A. Karim, F. Walter, D. M. Alexander, W. N. Brandt, C. de Breuck, E. da Cunha, S. C. Chapman, K. E. K. Coppin, A. L. R. Danielson, H. Dannerbauer, R. Decarli, T. R. Greve, R. J. Ivison, K. K. Knudsen, C. D. P. Lagos, E. Schinnerer, A. P. Thomson, J. L. Wardlow, A. Weiß, and P. van der Werf. An ALMA survey of sub-millimetre Galaxies in the Extended Chandra Deep Field South: the far-infrared properties of SMGs. *Monthly Notices of the Royal Astronomical Society*, 438:1267–1287, Feb 2014. (Cited on pages viii, 3, 4, 5, 6, and 12.)
- [42] A. M. Swinbank, J. M. Simpson, I. Smail, C. M. Harrison, J. A. Hodge, A. Karim, F. Walter, D. M. Alexander, W. N. Brandt, C. de Breuck, E. da Cunha, S. C. Chapman, K. E. K. Coppin, A. L. R. Danielson, H. Dannerbauer, R. Decarli, T. R. Greve, R. J. Ivison, K. K. Knudsen, C. D. P. Lagos, E. Schinnerer, A. P. Thomson, J. L. Wardlow, A. Weiß, and P. van der Werf. An ALMA survey of sub-millimetre Galaxies in the Extended Chandra Deep Field South: the far-infrared properties of SMGs. *Monthly Notices of the Royal Astronomical Society*, 438:1267–1287, Feb 2014. (Cited on page 12.)
- [43] L. J. Tacconi, R. Genzel, I. Smail, R. Neri, S. C. Chapman, R. J. Ivison, A. Blain, P. Cox, A. Omont, F. Bertoldi, T. Greve, N. M. Förster Schreiber, S. Genel, D. Lutz, A. M. Swinbank, A. E. Shapley, D. K. Erb, A. Cimatti, E. Daddi, and A. J. Baker. Submillimeter Galaxies at $z \sim 2$: Evidence for Major Mergers and Constraints on Lifetimes, IMF, and CO-H₂ Conversion Factor. *Astrophysical Journal*, 680:246–262, Jun 2008. (Cited on pages x, 9, 36, and 37.)
- [44] A. P. Thomson, R. J. Ivison, J. M. Simpson, A. M. Swinbank, I. Smail, V. Arumugam, D. M. Alexander, A. Beelen, W. N. Brandt, I. Chandra, H. Dannerbauer, T. R. Greve, J. A. Hodge, E. Ibar, A. Karim, E. J. Murphy, E. Schinnerer, S. Sirothia, F. Walter, J. L. Wardlow, and P. van der Werf. An ALMA survey of submillimetre galaxies in the Extended Chandra Deep Field South: radio properties and the far-infrared/radio correlation. *Monthly Notices of the Royal Astronomical Society*, 442:577–588, Jul 2014. (Cited on page 12.)
- [45] F. Walter, R. Decarli, M. Aravena, C. Carilli, R. Bouwens, E. da Cunha, E. Daddi, R. J. Ivison, D. Riechers, I. Smail, M. Swinbank, A. Weiß, T. Anguita, R. Assef, R. Bacon, F. Bauer, E. F. Bell, F. Bertoldi, S. Chapman, L. Colina, P. C. Cortes, P. Cox, M. Dickinson, D. Elbaz, J. González-López, E. Ibar, H. Inami, L. Infante, J. Hodge, A. Karim, O. Le Fevre, B. Magnelli, R. Neri, P. Oesch, K. Ota, G. Popping, H.-W. Rix, M. Sargent, K. Sheth, A. van der Wel, P. van der Werf, and J. Wagg. ALMA Spectroscopic Survey in the Hubble Ultra Deep Field: Survey Description. *Astrophysical Journal*, 833:67, Dec 2016. (Cited on page 8.)

- [46] S. X. Wang, W. N. Brandt, B. Luo, I. Smail, D. M. Alexander, A. L. R. Danielson, J. A. Hodge, A. Karim, B. D. Lehmer, J. M. Simpson, A. M. Swinbank, F. Walter, J. L. Wardlow, Y. Q. Xue, S. C. Chapman, K. E. K. Coppin, H. Dannerbauer, C. De Breuck, K. M. Menten, and P. van der Werf. An ALMA Survey of Submillimeter Galaxies in the Extended Chandra Deep Field-South: The AGN Fraction and X-Ray Properties of Submillimeter Galaxies. *Astrophysical Journal*, 778: 179, Dec 2013. (Cited on page 12.)
- [47] J. L. Wardlow, I. Smail, K. E. K. Coppin, D. M. Alexander, W. N. Brandt, A. L. R. Danielson, B. Luo, A. M. Swinbank, F. Walter, A. Weiß, Y. Q. Xue, S. Zibetti, F. Bertoldi, A. D. Biggs, S. C. Chapman, H. Dannerbauer, J. S. Dunlop, E. Gawiser, R. J. Ivison, K. K. Knudsen, A. Kovács, C. G. Lacey, K. M. Menten, N. Padilla, H.-W. Rix, and P. P. van der Werf. The LABOCA survey of the Extended Chandra Deep Field-South: a photometric redshift survey of submillimetre galaxies. *Monthly Notices of the Royal Astronomical Society*, 415:1479–1508, Aug 2011. (Cited on page 3.)
- [48] A. Weiß, A. Kovács, K. Coppin, T. R. Greve, F. Walter, I. Smail, J. S. Dunlop, K. K. Knudsen, D. M. Alexander, F. Bertoldi, W. N. Brandt, S. C. Chapman, P. Cox, H. Dannerbauer, C. De Breuck, E. Gawiser, R. J. Ivison, D. Lutz, K. M. Menten, A. M. Koekemoer, E. Kreysa, P. Kurczynski, H.-W. Rix, E. Schinnerer, and P. P. van der Werf. The Large Apex Bolometer Camera Survey of the Extended Chandra Deep Field South. *Astrophysical Journal*, 707:1201–1216, Dec 2009. (Cited on pages viii, 10, and 11.)
- [49] E. L. Wright. A Cosmology Calculator for the World Wide Web. *Publications of the ASP*, 118: 1711–1715, Dec 2006. (Cited on page 35.)